

The Physical Properties and Morphologies of Faint Dusty Star-forming Galaxies Identified with JWST

S. J. MCKAY ,¹ A. J. BARGER ,^{2,3,4} L. L. COWIE ,⁴ AND M. J. NICANDRO ROSENTHAL ²

¹Department of Physics, University of Wisconsin–Madison, 1150 University Avenue, Madison, WI 53706, USA

²Department of Astronomy, University of Wisconsin–Madison, 475 N. Charter Street, Madison, WI 53706, USA

³Department of Physics and Astronomy, University of Hawaii, 2505 Correa Road, Honolulu, HI 96822, USA

⁴Institute for Astronomy, University of Hawaii, 2680 Woodlawn Drive, Honolulu, HI 96822, USA

ABSTRACT

We develop a sample of 234 dusty star-forming galaxies (DSFGs) from the A2744 and GOODS-S fields using JWST/NIRCam-selected galaxies as priors for SCUBA-2 measurements. This provides a large number of galaxies both above an 850 μm flux of 2 mJy (47 bright DSFGs) and below (187 faint DSFGs). It represents the largest sample of individually identified (i.e., not stacked) faint DSFGs to date. We identify a tight negative correlation between redshift and both f_{F444W} and f_{F150W} , suggesting that the observed NIR flux may be an effective way of selecting high-redshift DSFGs. We study the physical properties of the DSFGs through spectral energy distribution fitting and morphological analysis. Other than the lower star formation rates (SFRs) and total infrared luminosities in the faint DSFGs, the two populations have similar properties. The stellar masses do not appear to be strongly dependent on either the SFRs or the submillimeter flux. These results suggest that the faint DSFGs are drawn from the same population of galaxies as the bright DSFGs. We find a lower merger fraction ($\sim 21\%$) relative to previous HST-based studies.

1. INTRODUCTION

It is well-established that a large fraction of the cosmic star formation history (SFH) is shrouded by dust, with estimates that dust-obscured star formation is more prevalent than unobscured star formation out to redshifts of at least $z \sim 4\text{--}5$ (e.g., Bouwens et al. 2020; Zavala et al. 2021; Sun et al. 2025). The most powerful individual contributors to the dust-obscured portion of the cosmic SFH are dusty star-forming galaxies (DSFGs), also called submillimeter galaxies (SMGs) due to their original discovery at 850 μm (Smail et al. 1997; Barger et al. 1998; Hughes et al. 1998; Eales et al. 1999).

While thousands of DSFGs have been detected through wide-field surveys with bolometer cameras on single-dish telescopes, the majority of these are brighter than $\sim 2\text{--}3$ mJy at 850 μm , i.e., above the confusion limits of single-dish submillimeter telescopes (~ 1.6 mJy for SCUBA-2 on the 15-m JCMT at 850 μm ; Cowie et al. 2017). Despite their extreme star formation rates (SFRs), which can exceed $\sim 1000 M_{\odot} \text{ yr}^{-1}$, bright DSFGs ($f_{850\,\mu\text{m}} > 2$ mJy) contribute only $\sim 20\text{--}30\%$ of the total star formation rate density (SFRD) above $z \sim 2$ due to their rarity (e.g., Barger et al. 2012, 2014; Cowie et al. 2017). However, faint DSFGs ($f_{850\,\mu\text{m}} < 2$ mJy),

which make up most of the dust-obscured SFH, have been much more difficult to study in large numbers.

Single-dish confusion noise prevents faint DSFGs from being directly selected for efficient followup with interferometers such as the Atacama Large Millimeter/submillimeter Array (ALMA) (e.g., Cowie et al. 2018). This necessitates selection using either direct interferometric surveys, which are costly and yield relatively small numbers of sources in limited areas (e.g., Walter et al. 2016; Aravena et al. 2016), or alternative techniques to probe beneath the confusion limit. These include taking advantage of the magnification from massive lensing clusters (e.g., Smail et al. 1997; Cowie et al. 2002, 2022; Knudsen et al. 2008; Chen et al. 2013; Hsu et al. 2016; Fujimoto et al. 2023, 2024), or using predetermined optical to near-infrared (NIR) color selections as priors for making measurements in submillimeter maps (e.g., Wang et al. 2012; Caputi et al. 2012; Chen et al. 2016; Wang et al. 2016, 2019; Barger & Cowie 2023; McKay et al. 2024). As a result, there only a handful of analyses of faint DSFG samples that have contrasted them with bright DSFG samples (e.g., Aravena et al. 2016; Chen et al. 2016; Cowie et al. 2022; Suzuki et al. 2023; Uematsu et al. 2024). However, these have been limited by their small sample sizes.

Added to these difficulties, studies of faint DSFGs suffer from the same limitations as those of bright DSFGs. Most critically, their optical/NIR counterparts are challenging to identify due to the $\sim 7\text{--}30''$ resolu-

Corresponding author: Stephen J. McKay
sjmckay3@wisc.edu

tion of single-dish submillimeter/millimeter telescopes. This hampers reliable estimates of their stellar masses and photometric redshifts. In addition, even when their precise positions are known, some show little to no optical emission (e.g., Chen et al. 2015; da Cunha et al. 2015; Cowie et al. 2018; Stach et al. 2019) at the typical depths of HST or ground-based surveys.

Finally, before the launch of JWST, high-resolution imaging redward of rest-frame $\sim 0.5 \mu\text{m}$ was not available for DSFGs above $z \sim 2$. Since the rest-frame optical/NIR traces the majority of the stellar mass, and stellar morphologies can help distinguish between merger-driven or secular star-formation triggering mechanisms, this prevented a full understanding of DSFGs' evolutionary pathways or the processes driving their SFRs. While deep HST observations at $1.6 \mu\text{m}$ suggested that DSFGs resembled large, massive disks, with high rates of mergers/irregular morphologies and spatial offsets between the UV/optical and submillimeter emission (Swinbank et al. 2010; Targett et al. 2013; Chen et al. 2015), there was some evidence that structured dust obscuration could be significantly impacting these rest-frame UV/optical morphologies. Now, JWST studies are placing stronger constraints on the stellar masses and morphologies of bright DSFGs (e.g., Chen et al. 2022; Gillman et al. 2023, 2024; Hodge et al. 2025), including detecting counterparts too faint for HST (e.g., Pérez-González et al. 2023; Xiao et al. 2024; Williams et al. 2024; Gottumukkala et al. 2024; Sun et al. 2024b); however, little is known about these properties for faint DSFGs.

Rather than simply analyzing the JWST data for known DSFGs, we can invert the process and use the JWST data to identify DSFGs. Barger & Cowie (2023) showed that red JWST/NIRCam F444W/F150W colors reliably identify NIR counterparts to SCUBA-2 $850 \mu\text{m}$ -selected DSFGs, building on past selections with HST and/or Spitzer (e.g., Wang et al. 2012; Caputi et al. 2012; Chen et al. 2016; Wang et al. 2016, 2019). They further showed that these red galaxies could be used as priors to identify SCUBA-2 $850 \mu\text{m}$ sources below the confusion limit. In McKay et al. (2024), we verified that this selection is highly accurate by demonstrating that $\sim 95\%$ of the red NIRCam galaxies with SCUBA-2 detections are also associated with $> 3\sigma$ ALMA detections. This procedure provides large, uniform samples of both bright and faint DSFGs with accurate JWST counterparts, making it possible to study how the two populations compare.

We apply the Barger & Cowie (2023) selection across the A2744 and GOODS-S fields to develop a large sample of $850 \mu\text{m}$ and/or 1.2 mm -detected DSFGs, most of which are fainter than 2 mJy at $850 \mu\text{m}$. In this paper, we focus on the stellar properties of these galaxies, which we measure from both integrated spectral energy distribution (SED) fits and surface brightness modeling.

In Section 2, we summarize the multiwavelength data in the A2744 and GOODS-S fields. In Section 3, we describe the NIRCam selection that we use to identify DSFGs, and we detail some initial characteristics of our sample. In Section 4, we fit the full optical-to-millimeter SEDs of the sample to constrain their stellar properties. We then describe the basic properties of the red DSFG sample derived from our SED fitting in order to understand the nature of the galaxies identified by our red NIRCam selection. We compare the properties of the faint DSFGs with those of the well-studied bright DSFGs. In Section 5, we analyze the surface brightness profiles of the DSFGs and investigate how many of them exhibit major merger signatures. Finally, in Section 6, we summarize our results.

Throughout the paper, we assume a flat concordance ΛCDM cosmology with $\Omega_m = 0.3$, $\Omega_\Lambda = 0.7$, and $H_0 = 70.0 \text{ km s}^{-1} \text{ Mpc}^{-1}$. We assume a Kroupa (2001) initial mass function (IMF). All magnitudes are quoted in the AB system (Oke & Gunn 1983).

2. DATA

2.1. A2744

The A2744 field has JWST observations from several surveys, including the GLASS-A2744 (Treu et al. 2022) and UNCOVER (Bezanson et al. 2024) programs. We use the catalog of isophotal photometry from Paris et al. (2023) for consistency with Barger & Cowie (2023), which includes eight bands of HST imaging in addition to the JWST data. We also make use of the additional data products provided for some sources by the UNCOVER team, such as lensing magnifications and photometric and spectroscopic redshifts (DR2; Weaver et al. 2024). The lensing magnifications are derived from the lensing model of Furtak et al. (2023a), which is highly constrained using both HST and JWST multiply imaged sources.

The SCUBA-2 data in A2744 were presented in Cowie et al. (2022) and discussed further in Barger & Cowie (2023) and McKay et al. (2024). The SCUBA-2 images are centered on the inner cluster region and have minimum 1σ rms noise values at $450 \mu\text{m}$ and $850 \mu\text{m}$ of 2.8 mJy and 0.26 mJy , respectively.

In addition to the previous ALMA coverage of the central A2744 cluster region from the 1.2 mm ALMA Lensing Cluster Survey (ALCS; Fujimoto et al. 2024) and the 1.1 mm ALMA Frontier Fields Survey (AFFS; González-López et al. 2017; Muñoz Arancibia et al. 2023) surveys, Fujimoto et al. (2023) recently published the Deep UNCOVER-ALMA Legacy High-Z (DUALZ) survey data and catalog, which covered a 24 arcmin^2 region corresponding to the UNCOVER NIRCam mosaic with 1.2 mm ALMA imaging down to a minimum rms value of $32.7 \mu\text{Jy}$. We use the data products from that survey, since they include the previous ALMA data in the field.

2.2. GOODS-S

We include the GOODS-S field in our study to take advantage of its extremely deep JWST and submillimeter/millimeter observations, along with unparalleled multiwavelength coverage from the X-ray to the radio.

We primarily use the JWST data from the JADES survey (Eisenstein et al. 2023a). We use the imaging and photometric catalog from the second data release (JADES DR2; Eisenstein et al. 2023b), which includes NIRCam photometry from the JEMS (Williams et al. 2024) and FRESCO (Oesch et al. 2023) surveys. We use the photometry measured in the largest Kron apertures (Kron parameter = 2.5) to recover the total fluxes. The JADES DR2 catalog also includes the HST photometry measured from the Hubble Legacy Field project (Illingworth et al. 2016; Whitaker et al. 2019).

The GOODS-S has extremely deep SCUBA-2 450 μm and 850 μm data, which have been extensively analyzed in Cowie et al. (2018), Barger et al. (2019), and Barger et al. (2022). The minimum 1σ rms noise values of the current 450 μm and 850 μm maps are 1.67 mJy and 0.18 mJy, respectively.

Portions of the GOODS-S have been observed by numerous ALMA programs covering a range of depths, frequencies, and beam sizes. Rather than re-reduce the data, we make use of published images or submillimeter/millimeter source catalogs, where possible. We use the ALMA 1.2 mm catalog from v2.0 of the GOODS-ALMA survey (Gómez-Guijarro et al. 2022) and the ALMA 1.2 mm catalog from the ASAGAO survey (Hatsukade et al. 2018). We also use the ALMA 870 μm , 1.2 mm, 2 mm, and 3 mm fluxes from Cowie et al. (2018) and McKay et al. (2023).

To search for fainter ALMA sources, we use the 26 arcmin² combined 1.2 mm continuum image (with a *uv*-taper of 250 k λ and primary beam correction applied) released by Hatsukade et al. (2018), who combined data from Dunlop et al. (2017) and Franco et al. (2018) to obtain a depth of $\sim 30 \mu\text{Jy}$. The resulting synthesized beam size of this image is $0''.59 \times 0''.53$.

Finally, when performing our SED fits, we use the Spitzer/MIPS 24 μm photometry from Elbaz et al. (2011) and the Herschel/PACS 100 and 160 μm and Herschel/SPIRE 250 and 350 μm photometry from the HerMES survey (Oliver et al. 2012). We do not use the SPIRE 500 μm data due to the low spatial resolution and large uncertainties, and because we have the deep SCUBA-2 450 μm data.

3. SAMPLE SELECTION

3.1. Red NIRCam Galaxies

The photometric selection outlined in Barger & Cowie (2023) for identifying DSFG counterparts is as follows:

$$\begin{cases} f_{\text{F444W}}/f_{\text{F150W}} > 3.5, \\ f_{\text{F444W}} > 1 \mu\text{Jy}. \end{cases} \quad (1)$$

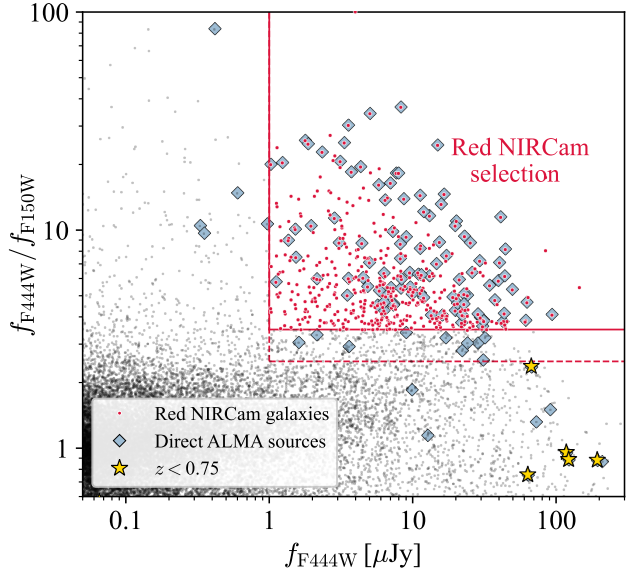


Figure 1. The red NIRCam galaxy selection (Equation 1; red solid lines) shown in $f_{\text{F444W}}/f_{\text{F150W}}$ color and f_{F444W} flux space. The sources from the Paris et al. (2023) and Eisenstein et al. (2023b) catalogs that satisfy this selection are shown as red points, while the remainder of the catalog sources are shown as black points. The ALMA 870 μm and/or 1.1/1.2 mm sources from Hatsukade et al. (2018), Cowie et al. (2018), Gómez-Guijarro et al. (2022), and Fujimoto et al. (2023) that have NIRCam counterparts are shown as blue diamonds (note that four sources lie off the lower left corner of the plot and may be spurious). ALMA sources with $z < 0.75$, including A2744 cluster members, are denoted by yellow stars. The red dotted lines illustrate an alternative selection with the color cut relaxed to $f_{\text{F444W}}/f_{\text{F150W}} > 2.5$. Note that the F444W fluxes for sources in A2744 have not been corrected for lensing.

We illustrate this red color selection in $f_{\text{F444W}}/f_{\text{F150W}}$ color and f_{F444W} flux space as the red solid lines in Figure 1. We plot all sources from the JADES DR2 or the GLASS-A2744 photometric catalogs (black points), marking those which satisfy Equation 1 (red points). We also show the ALMA 870 μm and/or 1.1/1.2 mm sources from Cowie et al. (2018), Hatsukade et al. (2018), Gómez-Guijarro et al. (2022), and Fujimoto et al. (2023) (blue diamonds). There are 132 unique ALMA sources from these surveys that lie on the F150W and F444W imaging. Two of these appear to match to red galaxies that are not deblended from brighter foreground objects in the JADES catalog, so we exclude them. Of the remaining 130 ALMA sources, 125 have clear ($f_{\text{F444W}} > 0.1 \mu\text{Jy}$) NIRCam counterparts at the ALMA position.

For the other 5 ALMA sources, one has no NIRCam counterpart within 1.5'', and four match to very faint ($f_{\text{F444W}} \lesssim 0.05 \mu\text{Jy}$), blue NIRCam sources; i.e., they

lie off the lower left side of Figure 1. All five of these objects are near the ALMA detection limits and are consistent with being spurious based on negative peak analyses in the original ALMA surveys, so we mark them as questionable and do not consider them further in our analysis.

We find that 100 out of 125 ALMA sources with robust NIRCam counterparts satisfy the criteria of Equation 1. Almost all of the 25 ALMA sources that do not satisfy the selection lie close to the selection boundary, being slightly fainter in F444W or slightly bluer in $f_{\text{F444W}}/f_{\text{F150W}}$. The ALMA detections that fall on the far lower right-hand side of Figure 1 mostly correspond to sources with $z < 0.75$ (yellow stars), including several A2744 cluster members.

It is clear from Figure 1 that although the red color selection is very effective at capturing the known ALMA detections, it is not complete. Excluding the five sources at $z < 0.75$, this selection captures $\sim 83\%$ of the known ALMA DSFGs with robust NIRCam counterparts. If we relaxed our selection to $f_{\text{F444W}}/f_{\text{F150W}} > 2.5$, $f_{\text{F444W}} > 1 \mu\text{Jy}$ (red dotted lines in Figure 1), we would recover an additional ten ALMA sources (110, or 92% of the total). However, in total, ~ 800 galaxies satisfy this relaxed selection, compared to ~ 450 galaxies that satisfy the original selection, meaning that the efficiency decreases drastically as we go to lower $f_{\text{F444W}}/f_{\text{F150W}}$ ratios. Thus, for this paper, as a good trade-off between achieving high completeness and high purity while also providing an efficient sample to use as priors in selecting faint DSFGs, we use the original selection from Barger & Cowie (2023).

To define our sample of red NIRCam galaxies, we begin by selecting all sources in either the JADES DR2 or the GLASS-A2744 photometric catalogs that satisfy Equation 1.

In A2744, the SCUBA-2 coverage does not extend all the way to the edge of the NIRCam mosaic, so we restrict our selection to the overlapping region. We also remove sources that have `FLAG = 1` in the Paris et al. (2023) catalog and combine multiple sources that correspond to a single galaxy. After making these changes, we find 158 total red NIRCam galaxies in A2744. The effective NIRCam+SCUBA-2 area from which these 158 galaxies are selected is 41.3 arcmin^2 , giving a surface density of 3.82 arcmin^{-2} .

In the GOODS-S, the JADES data include several regions where the NIRCam F150W imaging does not cover the entire F444W region. As a result, some sources in the catalog only partially lie on the F150W image and have inflated $f_{\text{F444W}}/f_{\text{F150W}}$ ratios due to the lower F150W fluxes. We visually inspect each source to make sure we are not including sources that fall off the edge of the F150W coverage. This leaves 295 sources that satisfy the red color-selection criteria and are not flagged. However, two sources correspond to the same galaxy, so we combine them, giving a total of 294 galaxies in the

GOODS-S. Since the NIRCam imaging we use covers an effective area of 63.4 arcmin^2 , this corresponds to a surface density of 4.64 arcmin^{-2} .

After combining the samples from both fields, we have a final catalog of 452 red NIRCam galaxies.

3.2. Submillimeter/millimeter Properties of Red NIRCam Galaxies

We next determine how many of the red NIRCam galaxies are associated with significant SCUBA-2 850 μm or ALMA continuum detections. The method we use for obtaining SCUBA-2 fluxes based on the prior positions follows that of Barger & Cowie (2023), which we briefly summarize here: We start by measuring the SCUBA-2 850 μm flux at the position of each red NIRCam galaxy position. Then, working down from brighter to fainter 850 μm fluxes, we extract the peak flux within $4''$ of each prior and clean the source from the SCUBA-2 image using the matched-filter point spread function (PSF) in order to limit contamination of fainter sources by the wings of brighter sources. We measure the rms noise at the position of each source.

We consider a galaxy to be detected in the SCUBA-2 850 μm data if it is associated with a $> 3\sigma$ SCUBA-2 source. As we showed in McKay et al. (2024), this method is capable of identifying the correct counterpart to SCUBA-2 850 μm sources with an accuracy of up to 95%, which is comparable to or better than a combined radio plus machine learning method prior to the launch of JWST (An et al. 2018).

Across both the A2744 and GOODS-S fields, there are 184 red NIRCam galaxies with $> 3\sigma$ SCUBA-2 850 μm detections. Of these, 33 have known ALMA 870 μm fluxes from Cowie et al. (2018), which we use in place of the SCUBA-2 850 μm fluxes for the rest of our analysis (hereafter, we will refer to both as 850 μm fluxes). We also include in our sample four red NIRCam galaxies with ALMA 870 μm fluxes but $< 3\sigma$ SCUBA-2 850 μm detections.¹

By running the same detection procedure on 1000 randomly selected positions in the SCUBA-2 850 μm images, we constrain the false positive fraction to be $\sim 10\%$, meaning that roughly 18 of our $> 3\sigma$ SCUBA-2 sources could be false positives. If we were to lower the SCUBA-2 detection threshold to 2σ , then we would find 257 red NIRCam galaxies with 850 μm detections; however, in this scenario, the false positive fraction increases to $\sim 20\%$.

¹ We note that there are two ALMA 870 μm sources from Cowie et al. (2018) (sources #1 and #29 in their Table 4) that do fall on the JADES F444W and F150W NIRCam imaging but are not included in our sample: Both objects are clearly red galaxies associated with the ALMA 870 μm emission but are blended with foreground galaxies in the JADES catalog. We exclude these objects from the red DSFG sample to ensure a uniform selection process.

In McKay et al. (2024), we used the red NIRCam galaxies as priors to recover faint ALMA 1.2 mm sources that were not bright enough to be directly detected in the ALMA images. We do the same here for sources that fall within either the DUALZ 1.2 mm *Wide* map (Fujimoto et al. 2023) in A2744 or the combined 1.2 mm image from Hatsukade et al. (2018) in the GOODS-S. We use the publicly available primary beam-corrected mosaics for both fields. For each prior position lying in one of these ALMA mosaics, we measure the 1.2 mm flux by finding the largest local peak within $1''.0$ of the NIRCam position. We estimate the rms noise by measuring the standard deviation in 5000 random pixels within $12''$ of the source, after masking out any $> 4\sigma$ peaks in the region. We consider a galaxy detected if the peak flux is more than $3\times$ the estimated rms noise; we adopt these peak fluxes and rms errors as our 1.2 mm fluxes and errors. However, for sources matching to the 1.1/1.2 mm ALMA catalogs in Section 3.1, we use the published fluxes.

In total, there are 234 red NIRCam galaxies with at least a $> 3\sigma$ detection at $850 \mu\text{m}$ and/or 1.1/1.2 mm. We hereafter refer to these galaxies as the *red DSFG sample*. This is the sample we focus on in the remainder of the paper. We summarize the red DSFG sample and the parent sample of red NIRCam galaxies in Table 1.

We emphasize that $\sim 60\%$ of the red DSFG sample are new DSFGs revealed by the JWST selection, rather than previously known ALMA sources. In Figure 2, we show $850 \mu\text{m}$ flux versus F444W flux for all 234 galaxies. Of these, 47 galaxies (20%) have $850 \mu\text{m}$ fluxes brighter than 2 mJy, while 187 (80%) have $850 \mu\text{m}$ fluxes or 3σ upper limits less than 2 mJy (we discuss the relative properties of these two subsets in Sections 4 and 5). The median $850 \mu\text{m}$ flux of the entire red DSFG sample is $\langle f_{850 \mu\text{m}} \rangle = 1.15 \text{ mJy}$.

In Table 2, we provide the full catalog of galaxies in the red DSFG sample, including source IDs, coordinates, redshifts, $850 \mu\text{m}$ and 1.2 mm fluxes and errors, and various properties we estimate from the SED fits and morphological analysis.

3.3. Comparison with Other Red Galaxy Selections

A growing number of studies using HST, Spitzer, and/or JWST data have indicated that massive galaxies appearing faint or undetected at optical/NIR wavelengths (sometimes called “HST-dark” or “OIR-dark”, with varying definitions) may contribute significantly to the stellar mass density and SFRD at $z > 3$ (e.g., Wang et al. 2012, 2016, 2019; Alcalde Pampliega et al. 2019; Manning et al. 2022; Barrufet et al. 2023; Gottumukkala et al. 2024; Williams et al. 2024; Xiao et al. 2023, 2024; Barrufet et al. 2025). These galaxies are predominantly dusty and star-forming (e.g., Wang et al. 2019; Yamaguchi et al. 2019; Pérez-González et al. 2023; Xiao

Table 1. Sample Summary

	GOODS-S	A2744	Total
Red NIRCam Galaxies	294	158	452
Red DSFG sample ^a	144	90	234
Red DSFG Sample			
$f_{850 \mu\text{m}} > 2 \text{ mJy}$	35	12	47
$f_{850 \mu\text{m}} < 2 \text{ mJy}$	109	78	187
Spectroscopic ^b redshifts	77	47	124

^aThe red DSFG sample refers to red NIRCam galaxies with $> 3\sigma$ $850 \mu\text{m}$ or 1.1/1.2 mm detections.

^bThis includes the HST and JWST grism redshifts (see Section 3.4).

Table 2. Catalog Description for the Red DSFG Sample

Column Name	Description
ID	Galaxy ID (field and number)
R.A.	Right Ascension (J2000)
Decl.	Declination (J2000)
z	Adopted redshift
z Type	0=Photometric, 1=Spectroscopic, 2=HST grism, 3=JWST grism
Ref.	Reference for spectroscopic/grism redshifts
$f_{850 \mu\text{m}} & \sigma_{850 \mu\text{m}}$	$850 \mu\text{m}$ flux and error
$f_{1.2 \text{ mm}} & \sigma_{1.2 \text{ mm}}$	1.2 mm flux and error
μ	Lensing magnification (for A2744)
SFR	Star formation rate [M_\odot/yr]
$\log(M_*/M_\odot)$	Stellar mass
A_V	V -band attenuation [mag]
$\log(L_{\text{IR}}/L_\odot)$	IR luminosity from 8–1000 μm
$\log(L_{\text{UV}}/L_\odot)$	Monochromatic 2800 Å luminosity
n_{F444W}	Sérsic index at 4.4 μm
n_{F150W}	Sérsic index at 1.5 μm
$R_e, \text{F444W}$	Effective radius at 4.4 μm [kpc]
$R_e, \text{F150W}$	Effective radius at 1.5 μm [kpc]

NOTE—All fluxes and properties have been corrected for magnification in A2744. The full catalog is available in machine-readable format in the online journal. We only include a summary of the contents here for brevity.

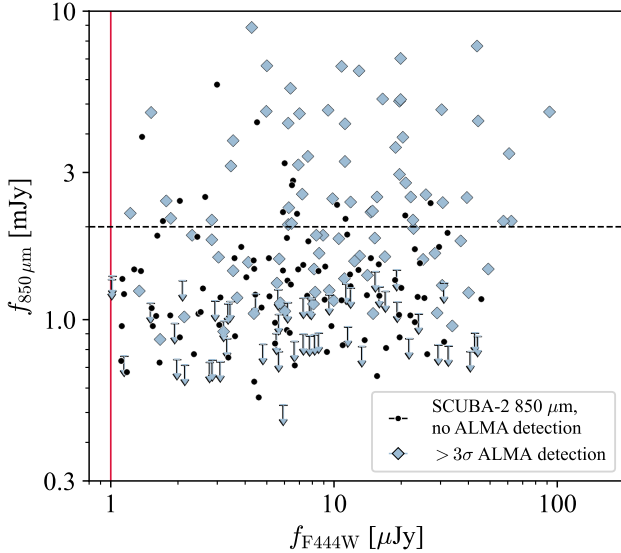


Figure 2. 850 μm flux vs. F444W flux for the red DSFG sample, distinguishing between sources with at least a $> 3\sigma$ ALMA detection (light blue diamonds) and those with $> 3\sigma$ SCUBA-2 850 μm detections but either no ALMA coverage or no ALMA detection (black points). For sources with $< 3\sigma$ SCUBA-2 850 μm detections (note that these have $> 3\sigma$ ALMA 1.1/1.2 mm detections), we show the 3σ upper limits (downward facing arrows). We mark our selection criterion of $f_{\text{F}444\text{W}} > 1 \mu\text{Jy}$ (red solid line). We also show the $f_{850\,\mu\text{m}} = 2 \text{ mJy}$ threshold between bright and faint DSFGs (black dashed line). Note that fluxes for sources in the A2744 field have not been corrected for lensing magnification.

et al. 2023; Barrufet et al. 2025), determined either by a combination of strong H α detections and reddened optical slopes, or by detections with SCUBA-2 or ALMA, though $\sim 10\text{--}20\%$ have been identified as massive quiescent galaxies (Pérez-González et al. 2023; Barrufet et al. 2025).

As the sample of DSFGs studied in this paper are also selected through red NIR colors, it is worth understanding how our sample compares with these populations. For clarity, we define *OIR-faint* to refer to galaxies with $f_{\text{F}444\text{W}}/f_{\text{F}150\text{W}} > 6.9$ and $f_{\text{F}150\text{W}} < 0.36 \mu\text{Jy}$ (25 mag), and we use *OIR-dark* to refer to the subset with $f_{\text{F}444\text{W}}/f_{\text{F}150\text{W}} > 6.9$ and $f_{\text{F}150\text{W}} < 0.14 \mu\text{Jy}$ (26 mag). These definitions correspond to the selections used in Gottumukkala et al. (2024) (see also, e.g., Pérez-González et al. 2023).

In Figure 3, we contrast the red NIRCam galaxy selection criteria shown in Figure 1 (red solid lines; Equation 1) with the OIR-faint and OIR-dark selection criteria (black dashed lines). We show the red DSFG sample with dark blue circles. Of the 234 sources in the red DSFG sample, a total of 35 (15%) are OIR-faint, with 16 of these being OIR-dark.

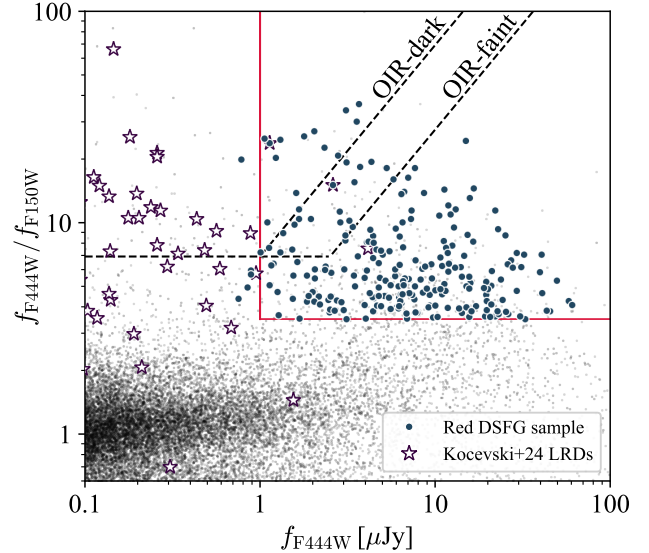


Figure 3. The $f_{\text{F}444\text{W}}/f_{\text{F}150\text{W}}$ colors and $f_{\text{F}444\text{W}}$ fluxes of the red DSFG sample (dark blue points). We show the color selections for OIR-faint and OIR-dark galaxies (black dashed lines; Gottumukkala et al. 2024). LRDs from Kocevski et al. (2024) in the A2744 and GOODS-S fields are shown as purple stars. We show the remaining sources in the Paris et al. (2023) and Eisenstein et al. (2023b) NIRCam catalogs as black points. Note that here, unlike Figure 1, the $f_{\text{F}444\text{W}}$ fluxes for sources in A2744 have been corrected for lensing.

The 35 OIR-faint DSFGs comprise 53% of the total number of red NIRCam galaxies that are OIR-faint. This is similar to the fraction of DSFGs in the total red NIRCam selected galaxy population.

However, below $f_{\text{F}444\text{W}} = 1 \mu\text{Jy}$, there are very few DSFGs, as was first shown by Barger & Cowie (2023) for $f_{\text{F}444\text{W}} \geq 0.05 \mu\text{Jy}$. This is consistent with the picture put forth by, e.g., Gottumukkala et al. (2024), in which the majority of the OIR-dark galaxies are “normal” star-forming galaxies with significant dust obscuration, whose SFRs would not be high enough to be detected via their cold dust emission by typical submillimeter/millimeter surveys.

A second red population that we can compare with our selection is “little red dots” (LRDs), a class of objects revealed by JWST that typically display compact morphologies and characteristic V-shaped SEDs in the rest-frame optical (though the exact definition varies; e.g., Furtak et al. 2023b; Kokorev et al. 2023; Matthee et al. 2024; Kocevski et al. 2024; Greene et al. 2024; Taylor et al. 2024; Labbe et al. 2025). Some of these seem to host moderate-luminosity broad-line active galactic nuclei (AGNs; for which hot dusty torus emission can produce a steep red rest-frame optical/NIR slope), despite showing only very marginal X-ray emission in deep stacked data (e.g., Ananna et al. 2024).

Nearly all the DSFGs are spatially extended in $f_{\text{F}444\text{W}}$, so we do not expect there to be any substantial overlap with the LRD samples. To illustrate this, we use the catalog of LRDs compiled by Kocevski et al. (2024), who selected compact JWST sources with red optical and blue UV slopes from several legacy field LRD samples. There are 69 sources in their sample across the GOODS-S and A2744 fields, which we plot on Figure 3 (purple stars). The LRDs generally have similar $f_{\text{F}444\text{W}}/f_{\text{F}150\text{W}}$ colors but fainter F444W fluxes than the red DSFG sample. This is not by construction, but reflects a real distinction between the populations. LRDs also tend to lie at $z > 3$, while the red DSFG sample (and the DSFG population in general) peaks around $z \sim 2.5$ (see Section 3.4).

Cross-matching the red DSFG sample to the Kocevski et al. (2024) catalog, we find that just two of our red DSFGs are also selected as LRDs (two other red NIRCam galaxies without submillimeter detections are also matched to their catalog, though one of these lies outside the red lines in Figure 3 after the magnification correction). One of these matched DSFGs is also the only X-ray source among the LRD sample in the GOODS-S ($L_X \sim 10^{44}$; see Kocevski et al. 2024 for an extended discussion of this source). In the mid- to far-infrared (FIR), this source is detected in Spitzer/MIPS and SCUBA-2 850 μm data ($f_{850\mu\text{m}} = 1.26 \text{ mJy}, \sim 3.1\sigma$).

A stacking of the remaining LRD positions in the SCUBA-2 850 μm data results in a stacked flux of $f_{850\mu\text{m}} = -0.056 \pm 0.043 \text{ mJy}$. Thus, the majority of LRDs are not DSFGs, even down to faint submillimeter fluxes, in agreement with the stacking analysis of Labbe et al. (2025) of 20 sources with ALMA 1.2 mm coverage in A2744.

3.4. Redshifts

We compile spectroscopic redshifts from the literature for the sources in the red DSFG sample, where available.

In the GOODS-S, these redshifts are taken from a variety of surveys and previously compiled catalogs (Mignoli et al. 2005; Vanzella et al. 2008; Kurk et al. 2013; Le Fèvre et al. 2015; Kriek et al. 2015; Inami et al. 2017; Cowie et al. 2018; McLure et al. 2018; Pentericci et al. 2018; González-López et al. 2019; Garilli et al. 2021; Bacon et al. 2023; Cowie et al. 2023; McKay et al. 2023), as well as JWST/NIRSpec programs (Bunker et al. 2024; D'Eugenio et al. 2024). For two sources, we adopt spectroscopic redshifts obtained from our own Keck/MOSFIRE observations. We also include HST grism redshifts from the 3D-HST program (Momcheva et al. 2016), though we note that these tend to be more uncertain than other spectroscopic or JWST grism redshifts.

In A2744, the spectroscopic redshifts come mainly from the ALT JWST/NIRCam grism program of Naidu et al. (2024) and the UNCOVER JWST/NIRSpec program of Price et al. (2024). We limit the Price et al.

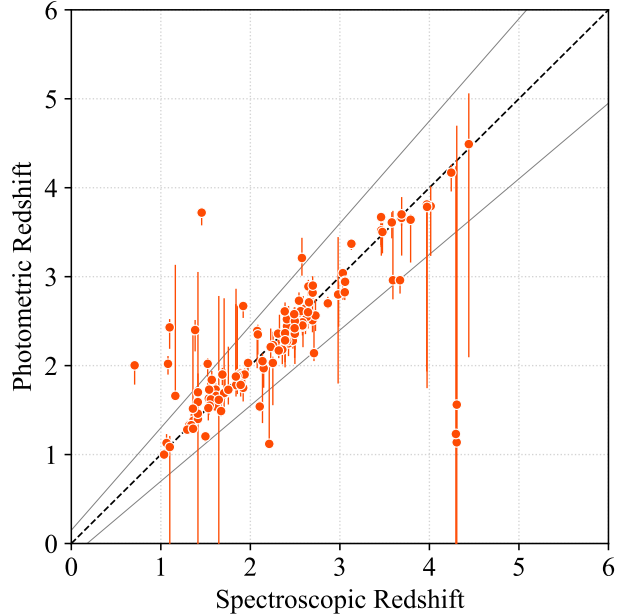


Figure 4. Photometric redshift from EAZY (error bars are the 16th–84th percentile ranges of the posteriors) vs. spectroscopic redshift (including HST grism) for sources in the red DSFG sample with spectroscopic redshifts (orange points). We also show the one-to-one correlation (black dashed line) and the $|z_{\text{spec}} - z_{\text{phot}}|/(1 + z_{\text{spec}}) = 0.15$ threshold (gray solid lines). 87% of the sources fall within this threshold.

(2024) redshifts to those with quality flag $q = 3$. We also include literature redshifts from the compilations of Muñoz Arancibia et al. (2023) and Sun et al. (2022) (the redshifts for these three sources come from ALMA program #2017.1.01219.S; PI: F. Bauer). Finally, we include six spectroscopic redshifts obtained from our Keck/MOSFIRE observations.

In total, 124 galaxies (53%) in the red DSFG sample have spectroscopic or grism redshifts; of these, 32 are HST grism redshifts. For all but four of the remaining 110 sources without spectroscopic or grism redshifts, we adopt photometric redshifts from the EAZY code, published in the Eisenstein et al. (2023b) and Weaver et al. (2024) catalogs. These redshifts are measured using just the HST and JWST photometry in each field. In Section 4.2, we discuss the four cases where there is no EAZY redshift or where we adopt a different redshift.

In Figure 4, we compare the photometric redshifts to the spectroscopic redshifts for the sources that have both. The accuracy of the photometric redshifts in predicting the true redshifts is very high, with 87% of the sources having $|z_{\text{spec}} - z_{\text{phot}}|/(1 + z_{\text{spec}}) < 0.15$ and 91% having $|z_{\text{spec}} - z_{\text{phot}}|/(1 + z_{\text{spec}}) < 0.20$.

In Figure 5, we show the final redshift distribution of the red DSFG sample. In the top panel, we show the breakdown of photometric versus spectroscopic/grism

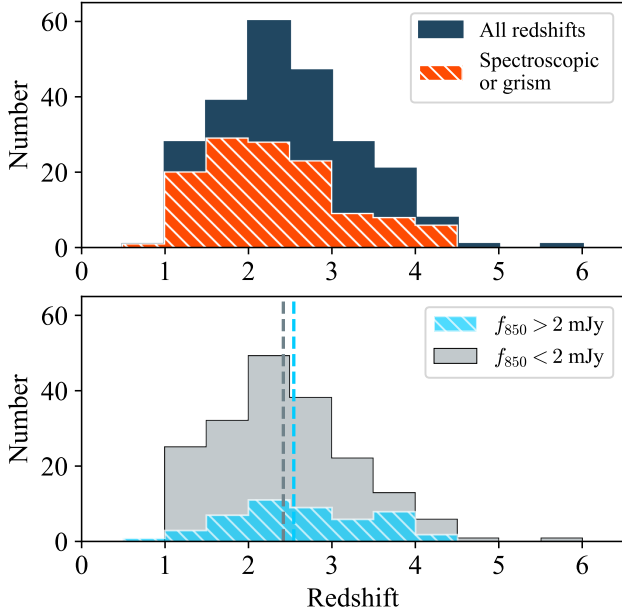


Figure 5. Top: Distribution of the best available redshifts for the red DSFG sample (dark blue), including adopted photometric redshifts, compared with the distribution of only spectroscopic/grism redshifts (hatched orange). Bottom: Comparison of redshift distributions for the $f_{850\text{ }\mu\text{m}} < 2 \text{ mJy}$ (gray histogram) and $f_{850\text{ }\mu\text{m}} > 2 \text{ mJy}$ (hatched light blue histogram) subsets. We also show the median redshifts of $\langle z \rangle = 2.42$ for the $f_{850\text{ }\mu\text{m}} < 2 \text{ mJy}$ subset (gray dashed line) and $\langle z \rangle = 2.54$ for the $f_{850\text{ }\mu\text{m}} > 2 \text{ mJy}$ subset (light blue dashed line).

redshifts, while in the bottom panel, we show the redshift distributions for the galaxies with $f_{850\text{ }\mu\text{m}} > 2 \text{ mJy}$ and $f_{850\text{ }\mu\text{m}} < 2 \text{ mJy}$, respectively. The faint DSFGs show no sign of having a different redshift distribution than the bright DSFGs. We will come back to this in Section 4.

The median redshift of the full red DSFG sample is $\langle z \rangle = 2.43$, with a 16th–84th percentile range of $z = 1.57\text{--}3.46$. This is in good agreement with other samples of 850 μm -selected DSFGs (e.g., Chapman et al. 2005; Danielson et al. 2017; Cowie et al. 2018; Dudzevičiūtė et al. 2020).

In Figure 6, we show how the F444W flux, F150W flux, and F444W/F150W flux ratios of the red DSFG sample vary with redshift. This demonstrates that both f_{F444W} and f_{F150W} have a strong negative correlation with redshift. The reason for the relationship is that we are seeing the tip of the luminosity function at any given redshift (Naidu et al. 2024; A. Barger et al., in preparation). We also observe a correlation between the $f_{\text{F444W}}/f_{\text{F150W}}$ color and redshift, though there is a larger degree of scatter.

Our finding of a correlation between f_{F444W} and redshift agrees with the correlation found in Barger et al.

(2022) using Spitzer/IRAC 4.5 μm fluxes for 450 μm -selected DSFGs. The best-fit line for our $f_{\text{F444W}} - z$ correlation is

$$z = (-1.48 \pm 0.14) \log(f_{\text{F444W}}) + (3.80 \pm 0.15), \quad (2)$$

with f_{F444W} in μJy . The best-fit line for our $f_{\text{F150W}} - z$ correlation is

$$z = (-1.27 \pm 0.11) \log(f_{\text{F150W}}) + (2.62 \pm 0.06). \quad (3)$$

The tightness of these correlations suggests that it may be possible to select high-redshift DSFGs based solely on their NIRCam 1.5 μm or 4.4 μm fluxes. It also suggests that rare $z > 5$ DSFGs may be inherently missed by our selection due to having fainter f_{F444W} or f_{F150W} .

4. PHYSICAL PROPERTIES FROM SED FITTING

4.1. SED Fitting with BAGPIPES

We fit the SEDs of the red DSFG sample with the BAGPIPES code, which uses a fully Bayesian framework to constrain the posterior likelihood distributions of the model parameters. When performing the SED fits, we consider all the available HST, JWST, Spitzer/MIPS, Herschel/PACS and SPIRE, SCUBA-2, and ALMA photometry, as described in Section 2 and Section 3.2. Before fitting the SEDs, we correct the observed A2744 photometry for lensing using the lensing magnifications published in Weaver et al. (2024). We also include a 5% error floor to ensure that the fits are not overly constrained by individual data points with very low rms errors.

For our SED models, we assume a delayed exponential SFH with ages between 1 Myr and 14 Gyr (in practice, the code restricts the model ages to less than the current age of the Universe at a given redshift) and τ ranging from 100 Myr to 9 Gyr. Variants of this form have often been used to model the SFHs of dusty galaxies (e.g., Wang et al. 2019; Barrufet et al. 2023, 2025; Yan et al. 2024; Pérez-González et al. 2024; Sun et al. 2024a) as it can account for both recent bursts and older generations of star formation.

We use a Calzetti et al. (2000) dust attenuation curve, which is a common choice for high-redshift studies (e.g., Lim et al. 2020; Barrufet et al. 2023; Xiao et al. 2023; Uematsu et al. 2024; Sun et al. 2024a). The magnitude of dust attenuation is parametrized by the V -band attenuation, A_V , which we allow to vary between 0 and 6; furthermore, we assume a factor of 2 higher attenuation in the stellar birth clouds. BAGPIPES uses the Bruzual & Charlot (2003) stellar population models and the dust emission models of Draine & Li (2007). The

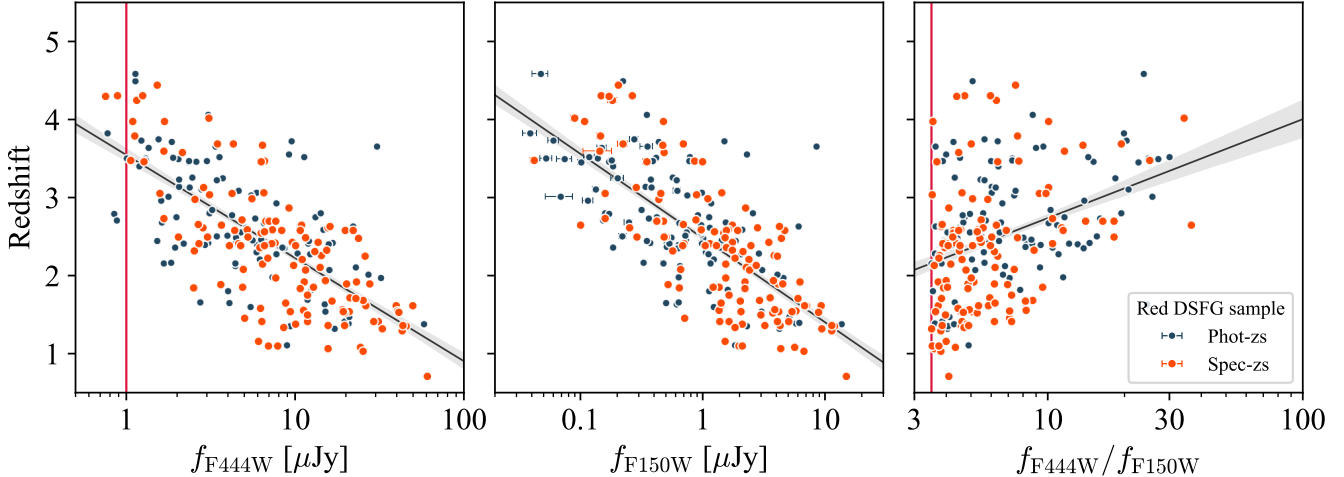


Figure 6. Redshift vs. $f_{\text{F}444\text{W}}$ (left), $f_{\text{F}150\text{W}}$ (center), and $f_{\text{F}444\text{W}}/f_{\text{F}150\text{W}}$ (right) for sources in the red DSFG sample, distinguishing between photometric redshifts (dark blue points) and spectroscopic redshifts (orange points). For each panel, we show the best-fit linear relationship (black line) and 16–84th percentile range on the fit (gray shaded region). In the left and right panels, we show the red color selection of Equation 1 (red solid line). Fluxes for sources in A2744 have been corrected for lensing. For most sources, the x-axis error bars are smaller than the data points.

stellar metallicity is allowed to range between 0.2 and 1.2 times solar metallicity. Finally, we include nebular emission based on the CLOUDY photoionization code (Ferland et al. 2017) with the ionization parameter $\log U$ fixed to -2.0 .

In the main BAGPIPES fits, we fix the model redshift to the best available redshift, prioritizing first spectroscopic and/or JWST grism redshifts, then HST grism redshifts, and, finally, photometric redshifts, as discussed in Section 3.4. Given the high accuracy of the EAZY redshift estimates (see Figure 4), we simply adopt these redshifts as the best photometric redshift estimate, except in four cases where we estimate the redshift with BAGPIPES (Section 4.2).

In Figure 7, we show examples of the best-fit SEDs for a representative subset of the red DSFG sample. In each panel, we also show a color image of the galaxy (R: F444W, G: F150W, B: F115W). We have chosen the examples to span a range of morphologies (major mergers, as well as isolated disks or spheroids), redshifts, and rest-frame optical SED shapes. Some of the sources are detected in up to ten FIR to millimeter bands, while others either are not covered by or are undetected in any FIR bands other than $850\ \mu\text{m}$, and, thus, would not otherwise have been identified as DSFGs.

We measure total SFRs for the red DSFG sample by converting their rest-frame UV and integrated IR luminosities from the best-fit BAGPIPES SEDs to SFRs following the prescription of Kennicutt (1998) (see also Bell et al. 2005), normalized to a Kroupa (2001) IMF. The total SFR is given by

$$\begin{aligned} \text{SFR} [\text{M}_\odot \text{ yr}^{-1}] = & 1.16 \times 10^{-10} L_{\text{IR}} \\ & + 3.35 \times 10^{-10} L_{\text{UV}}, \end{aligned} \quad (4)$$

where both L_{IR} and L_{UV} are in units of L_\odot . L_{IR} is integrated between rest-frame 8 to $1000\ \mu\text{m}$, and L_{UV} is computed as the monochromatic luminosity, νL_ν , at rest-frame $2800\ \text{\AA}$. We measure the flux at rest-frame $2800\ \text{\AA}$ using a top-hat filter with a width of $350\ \text{\AA}$ (e.g., Xiao et al. 2023) convolved with the best-fit BAGPIPES spectrum.

We do not correct L_{UV} for dust attenuation, since we use L_{IR} to trace the obscured star formation directly. Note that in our sample of dusty galaxies, the UV contribution to the SFR is typically dwarfed by the IR contribution ($L_{\text{IR}}/L_{\text{UV}} \sim 100$; see Table 3).

4.2. Testing Photometric Redshifts

The EAZY photometric redshifts from both Eisenstein et al. (2023b) and Weaver et al. (2024) are based only on HST and JWST data, so it is interesting to see whether the addition of the submillimeter/millimeter photometry helps to improve the photometric redshifts. We therefore perform a second round of BAGPIPES fits in which we allow the redshift to vary from $z = 0$ to $z = 14$ with a uniform prior. The constraints on the rest of the model parameters are treated identically to the SED fits in Section 4.1. We take the median of the posterior distribution as the BAGPIPES photometric redshift for each source.

In Figure 8, we show the difference between the BAGPIPES and EAZY photometric redshifts for the red DSFG sample. We also show the median and mean dif-

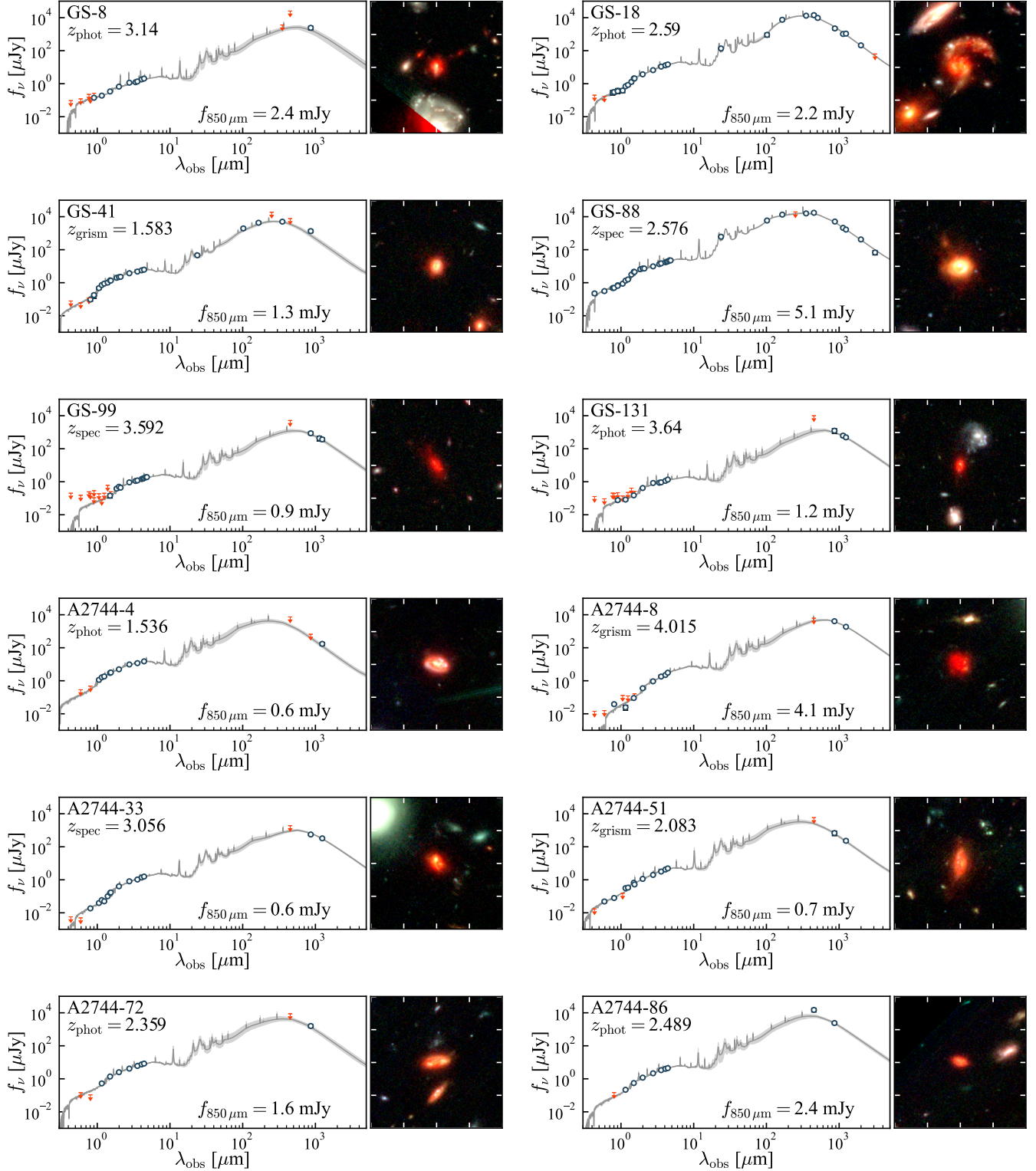


Figure 7. SED fits from **BAGPIPES** and RGB cutouts (R: F444W, G: F150W, B: F115W) for twelve example sources from the red DSFG sample. The cutouts are 8'' on a side. We show the observed photometry on the SED panels (dark blue circles if $>3\sigma$ detection; otherwise, red arrow for 3σ upper limit). The adopted redshifts (either spectroscopic, including HST grism, or photometric) and 850 μm fluxes (delensed for A2744) are marked on the SED panels.

ferences, both of which are close to zero. This implies

that both codes are in agreement for most of our sam-

Table 3. Median Properties of the Red DSFG Sample

	$f_{850\mu\text{m}} < 2 \text{ mJy}$	$f_{850\mu\text{m}} > 2 \text{ mJy}$	All
Number	187	47	234
z	$2.42^{+0.88}_{-0.87}$	$2.54^{+1.06}_{-0.88}$	$2.43^{+1.03}_{-0.86}$
$f_{850\mu\text{m}}$ [mJy]	$0.95^{+0.54}_{-0.54}$	$3.16^{+1.61}_{-0.86}$	$1.15^{+1.24}_{-0.63}$
$\log(M_*/M_\odot)$	$10.29^{+0.48}_{-0.39}$	$10.51^{+0.38}_{-0.46}$	$10.35^{+0.45}_{-0.42}$
SFR [$M_\odot \text{ yr}^{-1}$]	80^{+81}_{-45}	254^{+135}_{-131}	96^{+142}_{-56}
sSFR [Gyr^{-1}]	$0.53^{+0.49}_{-0.41}$	$0.94^{+0.56}_{-0.53}$	$0.57^{+0.63}_{-0.39}$
$\log(L_{\text{IR}}/L_\odot)$	$11.82^{+0.30}_{-0.36}$	$12.32^{+0.20}_{-0.30}$	$11.89^{+0.40}_{-0.36}$
$\log(L_{\text{UV}}/L_\odot)$	$9.89^{+0.38}_{-0.58}$	$9.93^{+0.59}_{-0.34}$	$9.89^{+0.41}_{-0.58}$
$\log(L_{\text{IR}}/L_{\text{UV}})$	$1.90^{+0.55}_{-0.29}$	$2.40^{+0.34}_{-0.57}$	$2.00^{+0.54}_{-0.35}$
A_V [mag]	$1.55^{+0.70}_{-0.37}$	$2.01^{+0.59}_{-0.65}$	$1.61^{+0.70}_{-0.42}$
n_{F444W}	$1.73^{+1.94}_{-0.83}$	$1.75^{+1.21}_{-0.81}$	$1.75^{+1.90}_{-0.85}$
n_{F150W}	$1.08^{+2.02}_{-0.62}$	$1.37^{+1.87}_{-0.93}$	$1.13^{+2.04}_{-0.67}$
$R_e, \text{F444W}$ [kpc]	$1.65^{+1.65}_{-1.01}$	$2.00^{+0.97}_{-0.90}$	$1.80^{+1.50}_{-1.10}$
$R_e, \text{F150W}$ [kpc]	$3.16^{+2.68}_{-1.77}$	$3.28^{+3.05}_{-1.51}$	$3.16^{+2.79}_{-1.74}$
(b/a) _{F444W}	$0.53^{+0.23}_{-0.25}$	$0.66^{+0.18}_{-0.23}$	$0.56^{+0.22}_{-0.26}$
(b/a) _{F150W}	$0.53^{+0.26}_{-0.26}$	$0.59^{+0.26}_{-0.30}$	$0.54^{+0.26}_{-0.27}$
Secure Merger %	$19 \pm 3\%$	$32 \pm 8\%$	$21 \pm 3\%$

NOTE—Median values and the 16th–84th percentile ranges (i.e., not the errors on the median), except for the secure merger fraction, where the errors are the Poisson errors. For sources in the A2744 field, all properties are corrected for lensing magnification. For the Sérsic index, effective radius, and axis ratio, we exclude sources flagged for poor **GALFIT** fits (see Section 5.1).

ple. There are clearly a number of outliers, for which the addition of the submillimeter data may be strongly influencing the final redshift estimate, but we do not observe an overall trend towards lower photometric redshifts in the **BAGPIPES** fits.

Although these **BAGPIPES** fits generally perform well in recovering the spectroscopic redshifts for sources that have both, the fraction with $|z_{\text{spec}} - z_{\text{phot}}|/(1 + z_{\text{spec}}) < 0.15$ is 80%, marginally lower than the **EAZY** results. This may be due in part to the choice of a uniform redshift prior (the **EAZY** fits use a more complex prior distribution).

However, there are four sources for which we adopt the **BAGPIPES** redshifts:

First, for one source (A2744-66) with no published **EAZY** redshift, we use the **BAGPIPES** redshift of $z_{\text{phot}} = 1.37$.

Second, the **EAZY** redshift for A2744-55 (a $f_{850\mu\text{m}} = 4.8$ mJy galaxy) is $z_{\text{phot}} = 0.197^{+0.004}_{-0.004}$, but the **BAGPIPES** best-fit redshift is $z_{\text{phot}} = 3.66^{+0.06}_{-0.08}$. This is also more consistent with the appearance of the source in the NIR-Cam image.

Next, there is a bright quasar (GS-59) with an X-ray detection ($L_X > 10^{43}$ erg/s) and **EAZY** $z_{\text{phot}} = 4.50^{+0.09}_{-0.30}$. This source is also detected by ALMA at 870 μm , 1.1 mm, 1.2 mm, and 2 mm. When fixed to the **EAZY** redshift, **BAGPIPES** suggests that this source is a $\log(L_{\text{IR}}/L_\odot) \sim 13$ galaxy with a stellar mass of $\log(M_*/M_\odot) \sim 11.8$. By contrast, when the redshift is allowed to vary, **BAGPIPES** converges on a much lower $z_{\text{phot}} = 1.63^{+0.13}_{-0.05}$ and does not find a secondary redshift solution at $z > 3$.

Finally, the source with the highest **EAZY** redshift in the sample is a GOODS-S galaxy (GS-144) at $z_{\text{phot}} = 11.21^{+0.36}_{-1.91}$. This source is coincident with a 2.4 mJy ALMA 870 μm source from Cowie et al. (2018) that is also detected in ALMA 1.2 mm and 2 mm imaging (McKay et al. 2023), and the **BAGPIPES** $z_{\text{phot}} = 3.01^{+0.08}_{-0.27}$. This is an example of a DSFG whose strong dust attenuation ($A_V \sim 3.1$) causes it to mimic the photometric colors of extremely high-redshift galaxies when only the optical to NIR photometry is considered (e.g., Naidu et al. 2022; Zavala et al. 2023; Meyer et al. 2024). In Figure 9, we show the two **BAGPIPES** fits for this galaxy: the first with the redshift fixed to the **EAZY**

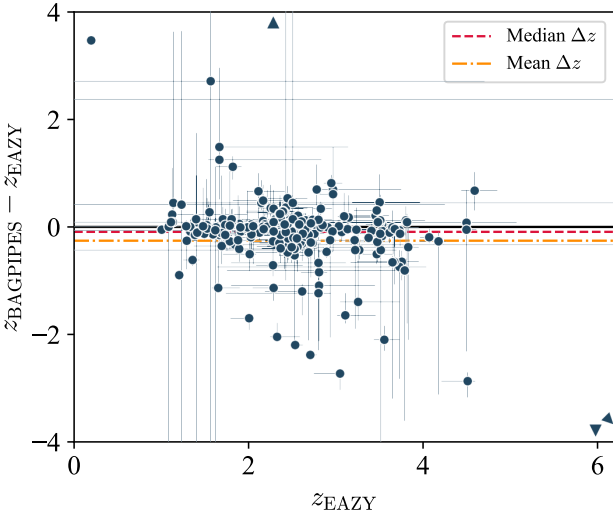


Figure 8. Difference between BAGPIPES and EAZY photometric redshifts for the red DSFG sample (dark blue points). The median (red dashed line) and mean (orange dash-dotted line) are shown for reference against the zero line (black solid line). Error bars refer to the 16th–84th percentile ranges on the individual redshift fits; the y-axis error bars incorporate both the BAGPIPES and EAZY errors. For three sources lying outside the plot range, we plot representative triangles indicating their relative positions.

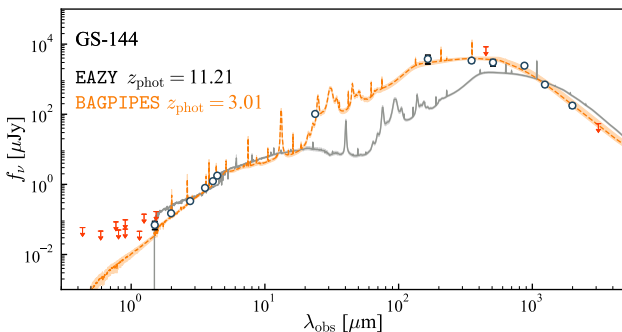


Figure 9. BAGPIPES SED fits for GS-144, the source with the highest EAZY photometric redshift in the red DSFG sample ($z_{\text{phot}} = 11.21$, measured using only the HST+JWST data), but which is also detected by ALMA at $870 \mu\text{m}$, 1.2 mm , and 2 mm . We show the BAGPIPES fits with the redshift fixed to the EAZY $z_{\text{phot}} = 11.21$ (gray solid line) and with the redshift allowed to vary (orange dashed line), resulting in $z_{\text{phot}} = 3.01$.

value, and the second where the redshift is allowed to vary.

We emphasize that adopting the BAGPIPES redshifts for these four sources has no significant impact on the median properties of our sample.

4.3. SED Results

In Figure 10, we plot histograms of the SFR, specific SFR ($\text{sSFR} \equiv \text{SFR}/M_*$), L_{IR} , and $L_{\text{IR}}/L_{\text{UV}}$ for the full red DSFG sample (open), as well as for the sample separated into $f_{850 \mu\text{m}} > 2 \text{ mJy}$ (hatched blue) and $f_{850 \mu\text{m}} < 2 \text{ mJy}$ (gray). We give the median values (dashed lines) in Table 3, along with the 16th–84th percentile ranges of the stellar masses, SFRs, dust attenuations, and IR and UV luminosities.

In general, we find that the galaxies in the full sample are best fit with a dusty SED model. For our assumption of a Calzetti et al. (2000) attenuation curve, we find $A_V = 1\text{--}3$ for almost all sources (median $A_V = 1.61$). The galaxies tend to be massive (median $\log(M_*/M_\odot) = 10.35$), and they lie between $1 \lesssim z \lesssim 5$. They have median $\log(L_{\text{IR}}/L_\odot) = 11.9$ and median $\text{SFR} = 96 M_\odot \text{ yr}^{-1}$. The sample spans over 2 dex in SFR and M_* , encompassing both moderately star-forming galaxies with SFRs as low as $5\text{--}50 M_\odot \text{ yr}^{-1}$ and extreme star-forming galaxies with SFRs up to $\sim 1000 M_\odot \text{ yr}^{-1}$.

As expected, the sources with $f_{850 \mu\text{m}} < 2 \text{ mJy}$ (80% of the sample) have substantially (~ 0.5 dex) lower SFRs and L_{IR} than those with $f_{850 \mu\text{m}} > 2 \text{ mJy}$. However, the stellar masses are not significantly different. A Mann-Whitney test indicates that the stellar mass distributions are only $\sim 2.1\sigma$ deviant from the hypothesis that they are drawn from the same parent distribution.

In terms of their SFRs alone, the faintest DSFGs overlap with the bright end of the extinction-corrected, UV-selected Lyman Break Galaxy (LBG) population (Cowie et al. 2017). However, we note that all but 14 (i.e., 94%) of the red DSFG sample have $L_{\text{IR}}/L_{\text{UV}} > 20$ (see Figure 10); i.e., their SFRs are completely dominated by dust-obscured star formation (traced by L_{IR}) rather than by unobscured star formation (traced by L_{UV}). Using the measured A_V , we correct the observed UV luminosities for dust and compare these to the SFRs based on both the IR and UV luminosities (i.e., our total SFR measured in Section 4.1). We find that the $\text{SFR}_{\text{UV,corr}}$ underpredicts the $\text{SFR}_{\text{IR+UV}}$ by a factor of 2.0, on average.

We next compare the properties of our sample with those of several DSFG samples for which SFRs and stellar masses have been published (we convert these to a Kroupa 2001 IMF). In Figure 11, we plot $f_{850 \mu\text{m}}$ versus SFR (left), stellar mass (center), and redshift (right). The comparison samples are the 99 sources in the main $f_{850 \mu\text{m}} \gtrsim 3.5 \text{ mJy}$ ALESS sample (da Cunha et al. 2015), the 707 sources in the $f_{850 \mu\text{m}} \gtrsim 2 \text{ mJy}$ AS2UDS sample (Dudzevičiūtė et al. 2020), the 289 sources in the SCUBADive sample (McKinney et al. 2025), and the 35 sources in the main ASPECS sample (Aravena et al. 2020).

We estimate $f_{850 \mu\text{m}}$ for ASPECS by converting their $f_{1.2 \text{ mm}}$ to $f_{850 \mu\text{m}}$ assuming a modified blackbody SED with $T = 35 \text{ K}$ and $\beta = 1.8$, a frequent choice in the

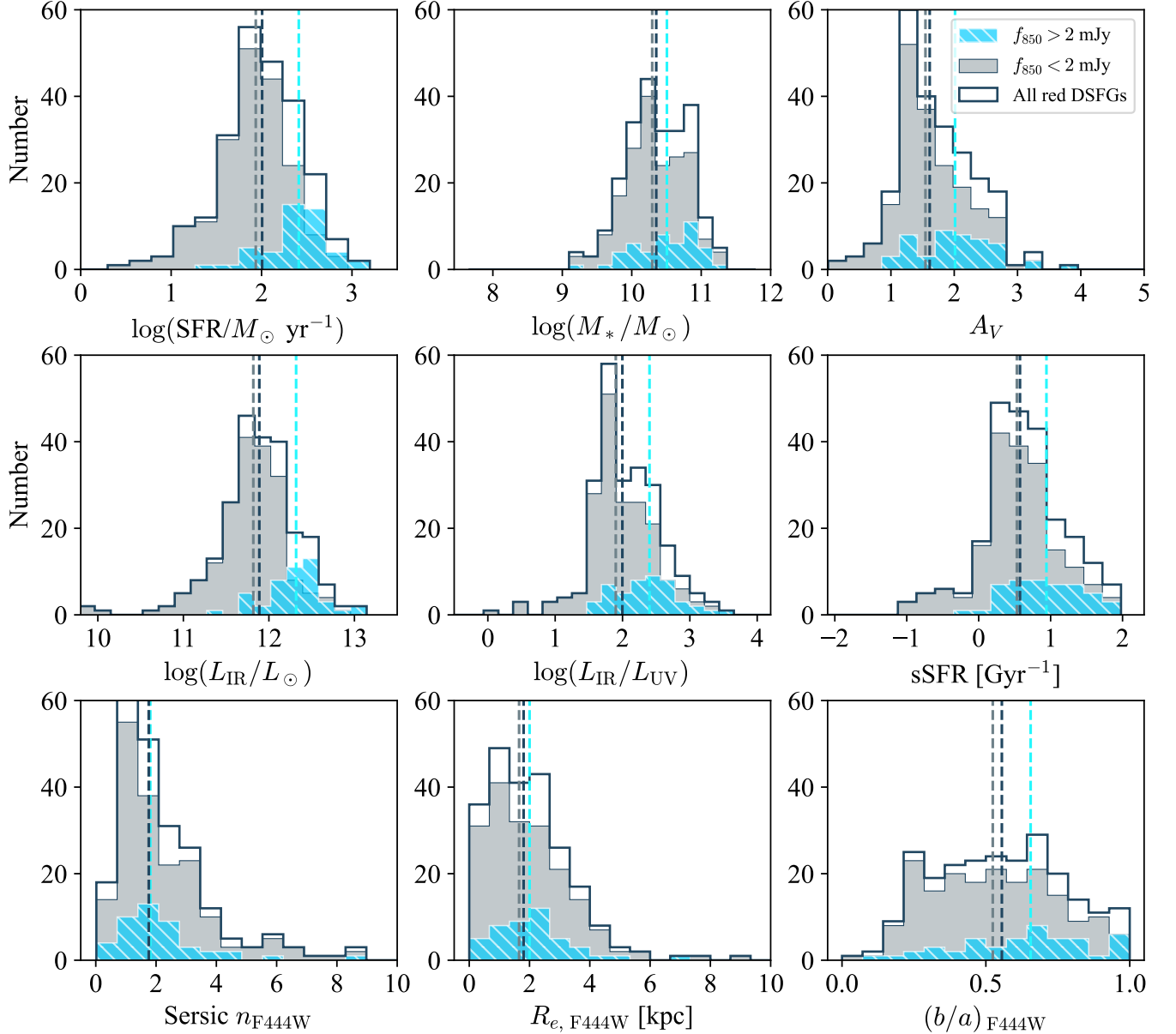


Figure 10. Distributions of the main physical parameters inferred from our SED and surface brightness profile fits for the red DSFG sample. We show the distributions for the full sample (open), as well as those for $f_{850\mu\text{m}} < 2 \text{ mJy}$ (gray) and $f_{850\mu\text{m}} > 2 \text{ mJy}$ (hatched blue). We show the median values as dashed lines. For the morphological parameters (Sérsic index, n ; effective radius, R_e ; and axis ratio, b/a), we exclude sources flagged for poor GALFIT fits (see Section 5.1).

literature. We note that using different assumptions on T and β within a range of reasonable values ($T = 20\text{--}55 \text{ K}$ and $\beta = 1.5\text{--}2.2$) do not produce more than a factor of 2 difference in the resulting $f_{850\mu\text{m}}$ values. Compared to the other surveys, ASPECS probes a much deeper flux regime ($\sigma_{1.2 \text{ mm}} = 9.3 \mu\text{Jy}/\text{beam}^{-1}$) over a much smaller area ($\sim 5 \text{ arcmin}^{-2}$). Aside from ASPECS, only a couple of ALMA surveys (e.g., ALCS, Fujimoto et al. 2024) have identified large DSFG samples at a similar flux range to that of our sample.

All of the galaxy properties of the literature samples were derived using a variant of the two-component Charlot & Fall (2000) attenuation curve, implemented in either the MAGPHYS (da Cunha et al. 2008) or CIGALE (Boquien et al. 2019) SED-fitting codes.² However, it has been shown that the choice of the Charlot & Fall

² A 0.2 dex offset was applied to the SCUBADive masses for consistency with the mass-to-light ratio in da Cunha et al. (2015); see McKinney et al. (2025)

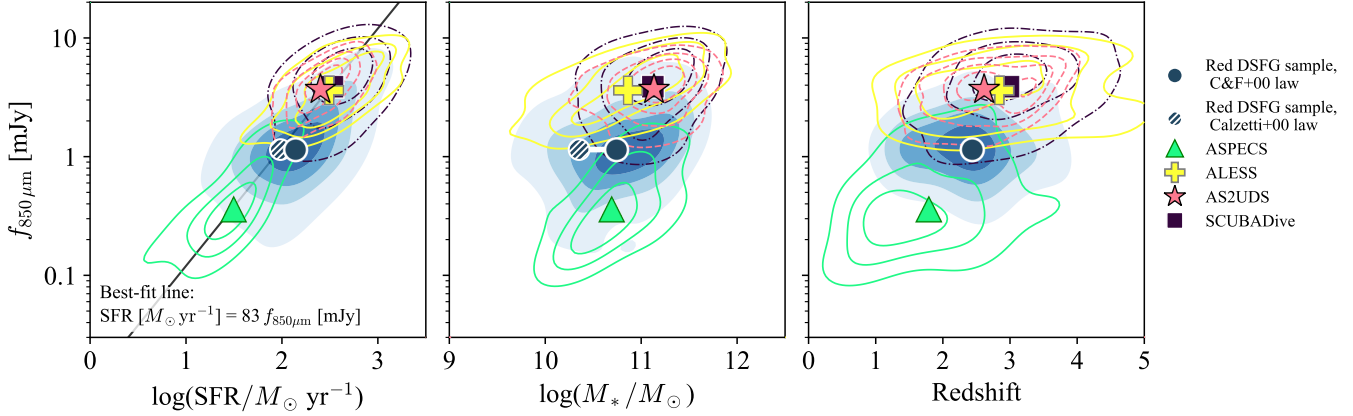


Figure 11. Comparison of derived properties assuming a Charlot & Fall (2000) attenuation curve for the red DSFG sample (blue circle and filled contours) with those of several literature samples: the ASPECS main sample (green triangle and solid contours; Aravena et al. 2020), ALESS SMGs (yellow cross and solid contours; da Cunha et al. 2015), AS2UDS SMGs (pink star and dashed contours; Dudzevičiūtė et al. 2020), and SCUBADive (purple square and dash-dotted contours; McKinney et al. 2025). For each sample, we plot the distribution of $f_{850\mu\text{m}}$ vs. SFR (left), stellar mass (center), and redshift (right) as Gaussian kernel density estimations, and we mark the median values (large symbols). We do not show the bootstrapped errors on the medians because they are generally smaller than the symbols. For sources with no direct $f_{850\mu\text{m}}$ measurement, we convert $f_{1.2\text{ mm}}$ to $f_{850\mu\text{m}}$ assuming a modified blackbody SED (see text). In the left and center panels, we also show the shift in median properties for our sample under our original assumption of a Calzetti et al. (2000) attenuation curve (hatched blue and white circle).

(2000) attenuation curve can increase stellar mass measurements by ~ 0.4 dex relative to the Calzetti et al. (2000) curve (e.g., Uematsu et al. 2024; see also Lo Faro et al. 2017).

For consistency, since BAGPIPES supports the use of dust attenuation curves, we reran our SED fits using the Charlot & Fall (2000) attenuation curve with a power-law slope of $\delta = -0.7$, in agreement with McKinney et al. (2025). In Figure 11, we show the properties derived from these fits, though we also plot the median values derived with the Calzetti et al. (2000) curve for comparison. The main effect of the Charlot & Fall (2000) model is to increase the measured stellar mass and A_V on average, since the shallower attenuation curve requires higher attenuation values to match the observed photometry. However, since BAGPIPES assumes energy balance between the UV/optical absorption and the IR emission, this also produces a ~ 0.15 dex increase in the L_{IR} , and therefore the SFR, on average. This highlights the need for caution when comparing properties derived from SED fits with different modeling assumptions (e.g., Michałowski et al. 2014; Lo Faro et al. 2017; Pacifici et al. 2023; Uematsu et al. 2024).

We see that the overall median SFR of the red DSFG sample is a factor of 2–3 lower than that of ALESS, AS2UDS, and SCUBADive (which all have median SFRs $\sim 300 M_\odot \text{ yr}^{-1}$) but above that of ASPECS (median SFR $\sim 30 M_\odot \text{ yr}^{-1}$). This reflects the fact that the $f_{850\mu\text{m}}$ range of our sample sits in between ASPECS and ALESS/AS2UDS/SCUBADive.

As has been seen previously for the bright DSFGs (e.g., Barger et al. 2014; Cowie et al. 2017), there is a close linear relation between the SFR and $f_{850\mu\text{m}}$. The left panel shows that this relation extends to the faint DSFGs. Considering all the DSFG samples, and weighting the fit by the individual errors on the data points, we find

$$\text{SFR} [M_\odot \text{ yr}^{-1}] = (83 \pm 11) \times f_{850\mu\text{m}} [\text{mJy}] \quad (5)$$

for the range 0.1 to 10 mJy (error is derived from bootstrapping the best-fit relation). The results remain unchanged if we restrict to $f_{850\mu\text{m}} > 2$ mJy. Our relation is slightly lower than the results of Barger et al. (2014), who found $\text{SFR} = 134 \times f_{850\mu\text{m}}$ (when converted to a Kroupa 2001 IMF), and of Cowie et al. (2017), who found $\text{SFR} = 143 \times f_{850\mu\text{m}}$. However, there are a variety of systematics involved that may be responsible for driving this difference; e.g., comparing SFRs derived from SED codes with those measured directly from IR luminosities. If we consider only the red DSFG sample, then the best-fit relation is $\text{SFR} = (132 \pm 18) \times f_{850\mu\text{m}}$, in agreement with the results of Barger et al. (2014) and Cowie et al. (2017) (all three of these studies used direct IR luminosity conversions to measure their SFRs).

We find a median stellar mass of $\log(M_*/M_\odot) = 10.74$ for the red DSFG sample. This is very close to the ASPECS result ($\log(M_*/M_\odot) \sim 10.65$). For the $f_{850\mu\text{m}} > 2$ mJy sources, we find $\log(M_*/M_\odot) = 10.94$, which is similar to those measured for ALESS (median $\log(M_*/M_\odot) \sim 10.9$), SCUBADive ($\log(M_*/M_\odot) \sim$

11.1), and AS2UDS ($\log(M_*/M_\odot) \sim 11.1$). The bootstrapped errors on the medians for these surveys range from 0.02–0.1 dex, and the statistical uncertainty associated with different models for the parametric SFH is ~ 0.1 –0.2 dex (e.g., Michalowski et al. 2014; Pacifici et al. 2023). Under our original choice of the Calzetti et al. (2000) curve, we measure a median stellar mass that is ~ 0.4 dex lower, but which is in good agreement with other color-based or NIR-dropout selections that employ similar modeling assumptions (e.g., Wang et al. 2019; Xiao et al. 2023; Pérez-González et al. 2023; Gotumukkala et al. 2024).

Finally, we find that the JWST data produce much lower statistical uncertainties on the stellar masses compared to previous studies that relied on HST and Spitzer/IRAC data. We find typical 1σ uncertainties of ~ 0.07 dex from the BAGPIPES fits, which are insignificant compared to the systematic modeling uncertainties discussed above. These can be compared to the ALESS 0.4–0.5 dex statistical uncertainties on the stellar mass, which are based on UV to NIR photometry from ground-based and Spitzer/IRAC observations.

5. MORPHOLOGIES AND MERGERS

In this section, we use the high resolution of the NIRCam data to characterize the average stellar morphologies of the red DSFG sample. We also investigate what fraction of these sources are undergoing major mergers, which have been proposed as a primary mechanism for triggering the extreme SFRs of DSFGs (e.g., Sanders & Mirabel 1996; Mihos & Hernquist 1996; Hopkins et al. 2008). We focus on the morphologies in the F150W and F444W bands. For the majority of our sample, these roughly correspond to the rest-frame optical and NIR, which, respectively, trace the young and old stellar populations.

5.1. Surface Brightness Profile Fitting

To measure the morphologies of the red DSFG sample, we use the GALFIT tool (Peng et al. 2002, 2010) to fit a two-dimensional (2D) parametric model to the images of each galaxy. GALFIT uses a nonlinear least-squares fitting process (built on the Levenberg-Marquardt algorithm) to determine the combination of parameters that minimizes the fit residuals, given a predetermined set of parametric models. It incorporates the instrumental PSF by convolving it with the provided model before fitting the data.

For our fits, we choose a single Sérsic profile, which is commonly used to model the light profiles of star-forming and passive galaxies in both the local Universe and at high redshifts (e.g., Wuyts et al. 2011; van der Wel et al. 2012; Kartaltepe et al. 2023). Although more complex models (e.g., multiple Sérsic profiles, or a Sérsic + point-source profile) are sometimes necessary to capture the detailed morphologies of star-forming galaxies,

they can overfit the data in some cases (e.g., Gillman et al. 2023).

We perform the fits on $8'' \times 8''$ cutouts of the F444W and F150W images centered on the NIRCam position of each galaxy. We perform simultaneous fits of any sources brighter than 26 mag and within $3''$ of the target galaxy (e.g., Nelson et al. 2023), but we use the segmentation maps provided by the respective JWST surveys to mask out other sources. The choice of F444W and F150W corresponds to the rest-frame optical and rest-frame NIR, respectively, for the majority of the red DSFG sample. Since the F444W data have higher signal-to-noise (S/N), we constrain the F150W Sérsic fits to have the same position angle as the best-fit F444W model. In both bands, we let GALFIT compute the noise image (including the sky background and shot noise) from the provided cutouts.

We produce an empirical PSF by stacking cutouts of bright, unsaturated stars selected from the NIRCam mosaics in each field. This method accounts for the observed broadening of the NIRCam PSF with respect to models (e.g., Nardiello et al. 2022; Zhuang & Shen 2024; Sun et al. 2024b; Weaver et al. 2024). We identify stars by selecting sources with `flag_star = 1` (or the equivalent) and $f_{\text{F444W}} > 1 \mu\text{Jy}$ in the respective JWST catalogs. We visually inspect them to ensure that the centers of the stars are not saturated in the relevant NIRCam filters and that the stars do not lie in a crowded field. We then stack the cutouts of the stars to generate the final PSF, which we pass to GALFIT to be convolved with the Sérsic model during the fitting.

In Figure 12, we present six examples of our GALFIT F444W and F150W fits. For galaxies in A2744, we correct all measured effective radii (i.e., half-light radii) for the lensing magnifications by scaling them by $1/\sqrt{\mu}$, where μ is the (2D) magnification factor. In Table 3, we give the median values and the 16th–84th percentile ranges of the Sérsic indices, effective radii, and axis ratios that we measure in F444W and F150W for the red DSFG sample. We also show the morphological parameters in Figure 10.

In many cases, the GALFIT residuals show substructure, such as spiral arms, clumps, or tidal features, that become more apparent once the Sérsic model has been subtracted from the image. This has also been noted by other recent studies of DSFGs (Le Bail et al. 2024; Polletta et al. 2024; Hodge et al. 2025; Price et al. 2025). Indeed, Jain & Wadadekar (2024) recently reported that one of the objects in our sample (A2744-53) is a grand design spiral at $z \sim 4$ (we find that this galaxy has a 3.2σ detection in the DUALZ ALMA data). The red DSFG sample also tend to appear clumpier at $1.5 \mu\text{m}$ than at $4.4 \mu\text{m}$, suggestive of structured dust obscuration that may drastically alter their morphologies between the rest-frame optical and NIR (e.g., Polletta et al. 2024; Gillman et al. 2024; Hodge et al. 2025).

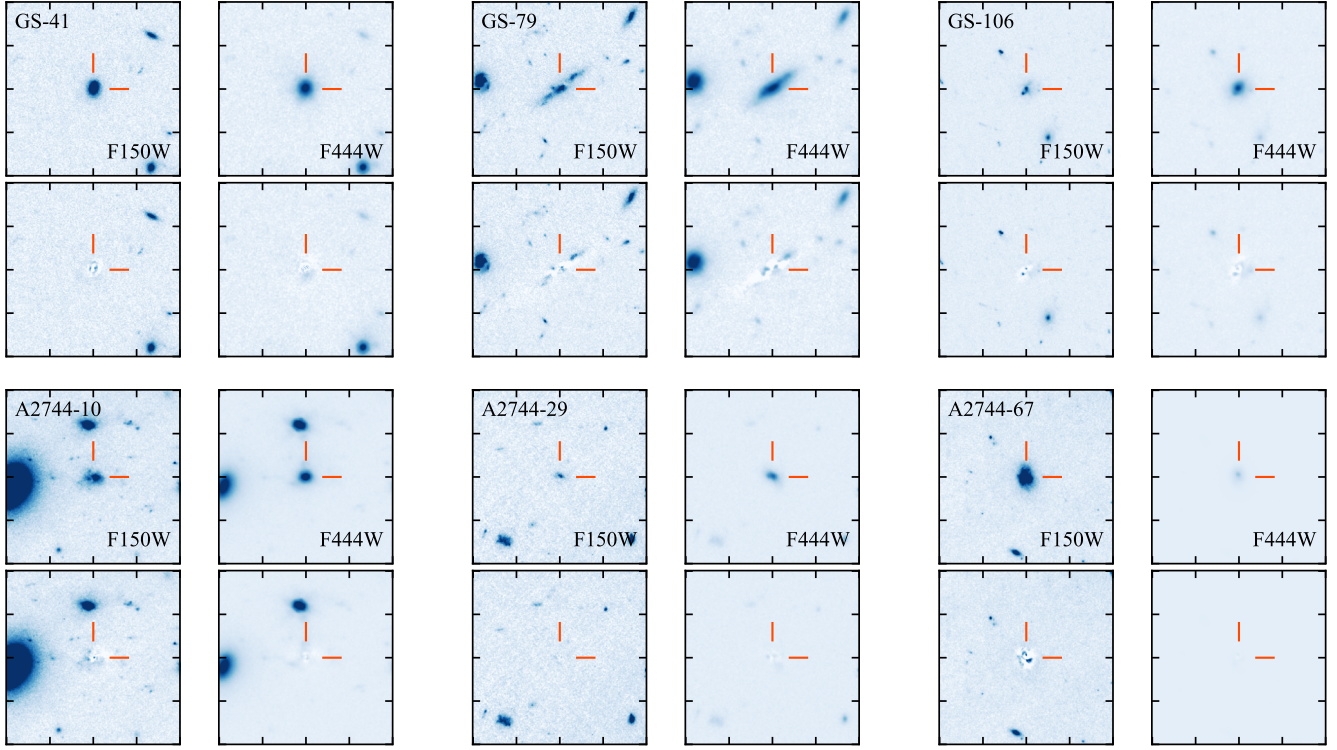


Figure 12. Surface brightness profile fitting results from `GALFIT` for six example sources from the red DSFG sample. For each source, we show the results for the F150W (left column) and F444W (right column) bands. For each band, we show the original image (top) and the residual image after subtracting the best-fit Sérsic profile (bottom). The images are 8'' on a side and centered on the NIRC positions (orange crosshairs).

We flag sources with measured $R_e > 50$ kpc, which is typically produced by low S/N detections in F150W or by nearby bright sources/mergers that influence the fit. The fraction of sources in the red DSFG sample with good fits that are not flagged in F444W is 98%, while in F150W it is 92% due to the fact that some sources have no F150W detection and hence cannot be modeled. We exclude these flagged objects from the median results quoted in Table 3 and from the histograms in Figure 10.

5.2. Identifying Mergers

Many previous studies indicated that DSFGs tend to exhibit disturbed morphologies and/or be engaged in some stage of a major merger. For example, in their sample of 48 ALMA-detected DSFGs, Chen et al. (2015) found a disturbed/merger incidence of $\sim 80\%$ and offsets between the rest-frame optical and FIR, from which they inferred that most DSFGs with $f_{850\mu\text{m}} > 2$ mJy are early/mid-stage mergers. Similarly, Franco et al. (2018) determined that $\sim 60\%$ of their sample of 18 DSFGs from the GOODS-ALMA survey had irregular morphologies or merger signatures.

However, these studies relied on HST data; thus, for $z > 2$, they were unable to probe the stellar light beyond rest-frame wavelengths of $\sim 0.5 \mu\text{m}$ and could be more impacted by dust attenuation. With the substantial in-

crease in sensitivity and wavelength coverage afforded by JWST, we can investigate the merger fraction of the red DSFG sample at longer rest-frame wavelengths with less susceptibility to the effects of dust.

To identify mergers, we perform visual inspections of each galaxy using 8'' \times 8'' RGB cutouts (R: F444W, G: F150W, B: F115W), along with the residual images from our `GALFIT` fits. We denote as “secure” (or major) mergers galaxies that exhibit clear signs of interactions, such as tidal tails, or that have close companions of similar colors. We denote as “tentative” mergers those that are, for example, located in a crowded field, or that have smaller companions (see, e.g., Gillman et al. 2024). In Figure 13, we show examples of each type of merger classification. We acknowledge that all visual classifications are inherently subjective; thus, while we should be able to identify major mergers with high reliability, there may be some minor mergers/interactions that we miss.

Among our sample, there are two separate pairs of red DSFGs where the galaxies appear to be merging with one another (we mark all four as secure mergers). There are a further eight red DSFGs that appear to be interacting with other galaxies in the red NIRC galaxy sample that were not selected as red DSFGs (i.e., the second galaxy does not have a submillimeter detection).

In total, we classify 50 ($21 \pm 3\%$) of the red DSFGs as secure mergers, and an additional 33 ($14 \pm 2\%$) as tentative mergers. These results are in line with some recent results from NIRCam data. For example, Cheng et al. (2023) reported that for their sample of 19 DSFGs with $f_{850\mu\text{m}} \sim 1\text{--}2 \text{ mJy}$, most galaxies exhibited nondisturbed, disk-dominated morphologies in the NIRCam F444W or F360M bands. Other NIRCam studies have reinforced this picture, with major merger fractions of $\sim 20\%$ and undisturbed disk morphologies comprising nearly half of the DSFG samples—consistent with non-DSFG field samples (e.g., Gillman et al. 2024). The implication seems to be that previous HST-based studies were more affected by dust attenuation, which can produce clumpy/disturbed-looking morphologies in sources that resemble smooth disks at longer wavelengths (e.g., Boogaard et al. 2024).

We note that Hodge et al. (2025) found that even in NIRCam data, $\sim 54 \pm 23\%$ of their sample of 12 DSFGs from ALESS displayed evidence for mergers/interactions, and only $\sim 23 \pm 8\%$ were classified as undisturbed disks. We argue that there are two reasons for this: First, the methods used to determine merger fractions vary from paper to paper: e.g., many authors combine major mergers and disturbed/irregular morphologies when reporting percentages, so comparing results is not always straightforward. If we combine our “secure” merger identifications with those marked as “tentative” (which may serve as a proxy for minor mergers or interactions), then we measure a total merger fraction of $\sim 35 \pm 4\%$ for the whole red DSFG sample.

Second, the Hodge et al. (2025) galaxies are, on average, much brighter DSFGs than ours (median $870\mu\text{m}$ fluxes of 6.4 mJy). Within our sample, we see hints that brighter $f_{850\mu\text{m}}$ correlates with higher merger fractions. For example, if we restrict to the 19 galaxies in the red DSFG sample with $f_{850\mu\text{m}} > 3.5 \text{ mJy}$ (even these only have a median $f_{850\mu\text{m}} = 4.7 \text{ mJy}$), then we measure a secure merger fraction of $37 \pm 14\%$, consistent with Hodge et al. (2025) within uncertainties. If we now combine the secure and tentative merger identifications in these 19 galaxies, then we measure a total merger fraction of $58 \pm 17\%$, in agreement with the Hodge et al. (2025) result.

5.3. Bulge Formation and Size Evolution

As can be seen from Figure 10 and Table 3, the Sérsic indices of the red DSFG sample fall mostly between $n = 0.5\text{--}4$, with median $n_{\text{F444W}} = 1.8$, suggestive of disk-dominated morphologies. The distribution of axis ratios that we measure (median $(b/a)_{\text{F444W}} = 0.56^{+0.22}_{-0.26}$ with a wide range from $(b/a) \approx 0.3\text{--}0.9$) are also generally consistent with a population of randomly oriented disks (e.g., Padilla & Strauss 2008; van der Wel et al. 2014; Tan et al. 2024). The brighter DSFGs are biased towards marginally higher (b/a) (see Figure 10), pos-

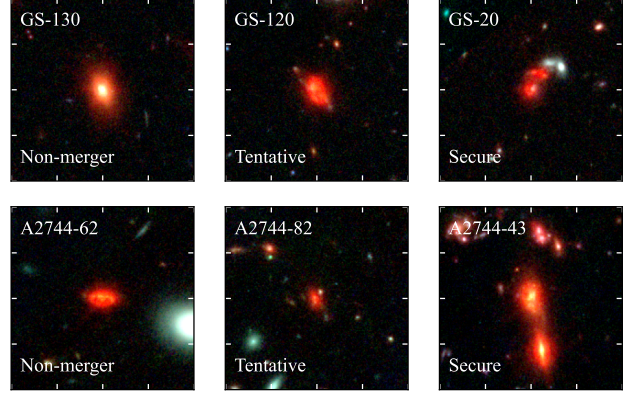


Figure 13. RGB cutouts (R: F444W, G: F150W, B: F115W) and merger classifications for six example sources from the red DSFG sample. The cutouts are $8''$ on a side.

sibly suggesting that their shapes or inclination angles differ slightly from the faint DSFGs, though our current sample is not sufficient to confirm this. Overall, we see no significant morphological differences between the $f_{850\mu\text{m}} > 2 \text{ mJy}$ and $f_{850\mu\text{m}} < 2 \text{ mJy}$ DSFGs.

However, the median effective radius in F150W of $R_{\text{e},\text{F150W}} = 3.16^{+2.79}_{-1.74} \text{ kpc}$ is substantially larger than the median effective radius in F444W of $R_{\text{e},\text{F444W}} = 1.80^{+1.50}_{-1.10} \text{ kpc}$ (also noted by, e.g., Chen et al. 2022; Gillman et al. 2023, 2024; Boogaard et al. 2024; Hodge et al. 2025; Price et al. 2025). The Sérsic indices in the rest-frame NIR are also somewhat higher (median $n_{\text{F444W}} = 1.75^{+1.90}_{-0.85}$) than those in the rest-frame optical (median $n_{\text{F150W}} = 1.13^{+2.04}_{-0.67}$).

The combination of smaller sizes and more compact light profiles at longer wavelengths suggests that the older stellar populations (traced by F444W) are more centrally concentrated than the younger populations (traced by F150W). In other words, we may be seeing an ongoing process of bulge formation in these galaxies, consistent with a picture of inside-out galaxy evolution (e.g., Kamieneski et al. 2023; Gillman et al. 2023). These trends may also reflect the impact of dust on the F150W morphologies—e.g., from an obscured central starburst—causing them to be less centrally concentrated and thereby lowering the Sérsic index and increasing the (measured) effective radius (see, e.g., Roper et al. 2022 and Nedkova et al. 2024).

To look for evolution in the average DSFG morphology, in Figure 14, we plot the measured effective radii (left) and Sérsic indices (right) in the F150W and F444W bands versus redshift. The large diamonds show the binned median values for the F150W (blue) and F444W (red) radii and Sérsic indices. We limit the redshift range for the bins to cover $1.25 \leq z \leq 3.5$, for which F150W probes the rest-frame optical and F444W probes the rest-frame NIR.

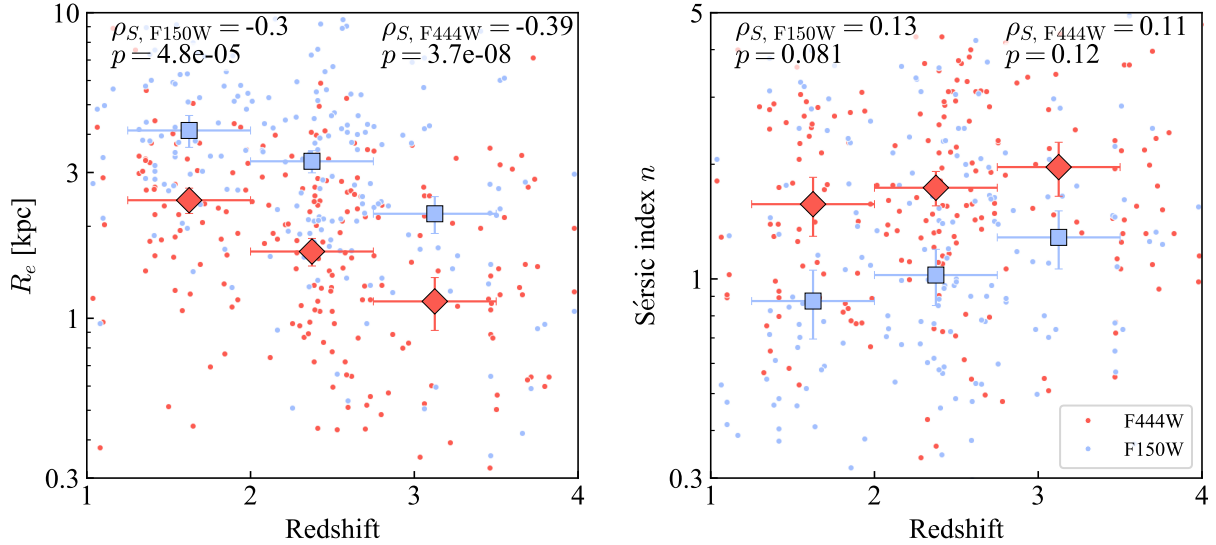


Figure 14. Effective radii (left) and Sérsic indices (right) vs. redshift for the red DSFG sample. We show measurements made in both the rest-frame optical (F150W; blue points) and rest-frame NIR (F444W; red points); i.e., each galaxy corresponds to two data points in each panel. The median effective radius and Sérsic index in several redshift bins are shown for F150W (blue squares) and F444W (red diamonds); for these, the horizontal error bars represent the bin width, and the vertical error bars are the bootstrapped error on the median. In the figure legend, we list the Spearman rank correlation coefficients and p -values for F150W and F444W, respectively.

In the left panel, we see a clear evolution in the median effective radius over the redshift range $z \sim 4$ to $z \sim 1$. We measure the Spearman rank correlation coefficient, ρ_S (a nonparametric indicator of the strength of the association between two variables), for both $R_{e, F150W}$ and $R_{e, F444W}$ and redshift, restricting to the redshift range above. The result is $\rho_{S, F150W} \approx -0.3$ (4.1σ) and $\rho_{S, F444W} \approx -0.4$ (5.5σ), indicating a moderately negative correlation between effective radius and redshift in each band. Most likely, this correlation simply reflects the growth of galaxy size over the course of cosmic noon (e.g., van der Wel et al. 2014), where dusty star formation is known to peak. A similar evolution in the stellar distributions of DSFGs was found by Gillman et al. (2023), though our sample size is $\sim 10\times$ larger.

In the right panel, we see an apparent increase in the median Sérsic index towards higher redshift. Combined with the trend towards smaller radii, this could indicate that DSFGs at higher redshift have slightly more compact profiles and have not yet formed large, exponential ($n \approx 1$) disks. However, in this case, the correlations between n_{F150W} and n_{F444W} and redshift are not statistically significant (1.7σ and 1.6σ , respectively), so more data are needed to assess whether this trend is real.

6. SUMMARY

Using JWST and SCUBA-2, we developed a large sample of 234 DSFGs covering a wide range of submillimeter fluxes. This allowed us to compare the properties of faint DSFGs ($f_{850\mu\text{m}} < 2$ mJy) with those of bright DSFGs ($f_{850\mu\text{m}} > 2$ mJy). We measured the stellar

properties using BAGPIPES SED fits and the morphologies using GALFIT. Our main results are as follows:

- Overall, the sample is made up of massive ($\log(M_*/M_\odot) \sim 10.3$), dusty ($A_V \sim 1.6$), highly star-forming ($\text{SFR} \sim 100 M_\odot/\text{yr}$) galaxies between $1 < z < 5$. We found that the SFRs are a linear function of submillimeter flux, extending the results of previous studies to fainter fluxes.
- The JWST data give small statistical errors on the stellar masses of the DSFGs. However, we found that the assumed dust attenuation curve has a significant impact on the measured stellar masses; for example, our use of Calzetti et al. (2000) results in ~ 0.4 dex lower stellar masses than Charlot & Fall (2000). When this is taken into account, our sample has similar stellar masses to other samples. Remarkably, nearly all of the DSFGs have similar masses regardless of their SFR or submillimeter flux.
- We identified a tight negative correlation between redshift and both f_{F444W} and f_{F150W} , suggesting that the observed NIR flux may be an effective way to select high-redshift DSFGs.
- Most of the galaxies in our sample appear to be isolated disks, with a moderately low fraction ($\sim 21\%$) clearly involved in major mergers. We argued that the high merger fractions quoted for DSFGs prior to JWST may have been due to strong

dust attenuation, which caused the images to appear clumpy at rest-frame optical wavelengths. However, we caution that different methods for identifying mergers can complicate the comparison of results between different studies.

- Between the rest-frame optical and NIR, the sample changes from extended ($R_e \sim 3.2$ kpc), exponential disk-like ($n \sim 1.1$) profiles to more compact ($R_e \sim 1.8$ kpc), slightly steeper ($n \sim 1.8$) profiles, suggesting the growth of stellar bulges and/or strong central dust attenuation.
- We found a moderate increase of R_e with decreasing redshift in both the rest-frame optical and NIR from $z = 4$ to $z = 1$, reflecting the build-up of galaxy size over the course of cosmic noon.

¹ S. J. M. thanks Jed McKinney for providing the derived properties and fluxes for the SCUBADive sample.

² We gratefully acknowledge support for this research from the William F. Vilas Estate (S. J. M.), a Kellett Mid-Career Award and a WARF Named Professorship from the University of Wisconsin-Madison Office of the Vice Chancellor for Research and Graduate Education with funding from the Wisconsin Alumni Research Foundation (A. J. B.), and NASA grant 80NSSC22K0483 (L. L. C.).

³ The National Radio Astronomy Observatory is a facility of the National Science Foundation operated under cooperative agreement by Associated Universities, Inc. This paper makes use of the following ALMA data:
⁴ ADS/JAO.ALMA#2013.1.00999.S,
⁵ ADS/JAO.ALMA#2015.1.01425.S,
⁶ ADS/JAO.ALMA#2015.1.00543.S,
⁷ ADS/JAO.ALMA#2015.1.00242.S,
⁸ ADS/JAO.ALMA#2015.1.00098.S,
⁹ ADS/JAO.ALMA#2017.1.01219.S,
¹⁰ ADS/JAO.ALMA#2017.1.00755.S,
¹¹ ADS/JAO.ALMA#2018.1.00035.L,
¹² ADS/JAO.ALMA#2021.1.00024.S.,
¹³ and ADS/JAO.ALMA#2022.1.00073.S.

¹⁴ ALMA is a partnership of ESO (representing its member states), NSF (USA), and NINS (Japan), together with NRC (Canada), MOST and ASIAA (Taiwan), and KASI (Republic of Korea), in cooperation with the Republic of Chile. The Joint ALMA Observatory is operated by ESO, AUI/NRAO, and NAOJ.

¹⁵ The James Clerk Maxwell Telescope is operated by the East Asian Observatory on behalf of The National Astronomical Observatory of Japan, Academia Sinica Institute of Astronomy and Astrophysics, the Korea Astronomy and Space Science Institute, the National Astronomical Observatories of China and the Chinese Academy of Sciences (grant No. XDB09000000), with additional funding support from the Science and Technology Facilities Council of the United Kingdom and participating universities in the United Kingdom and Canada.

¹⁶ We wish to recognize and acknowledge the very significant cultural role and reverence that the summit of Maunakea has always had within the indigenous Hawaiian community. We are most fortunate to have the opportunity to conduct observations from this mountain.

Facilities: ALMA, HST, JCMT, JWST

Software: astropy (Astropy Collaboration et al. 2022), BAGPIPES (Carnall et al. 2018), EAZY (Brammer et al. 2008), GALFIT (Peng et al. 2010), scipy (Virtanen et al. 2020)

REFERENCES

- Alcalde Pampliega, B., Pérez-González, P. G., Barro, G., et al. 2019, *ApJ*, 876, 135
- An, F. X., Stach, S. M., Smail, I., et al. 2018, *ApJ*, 862, 101
- Ananna, T. T., Bogdán, Á., Kovács, O. E., Natarajan, P., & Hickox, R. C. 2024, *ApJL*, 969, L18
- Aravena, M., Decarli, R., Walter, F., et al. 2016, *ApJ*, 833, 68
- Aravena, M., Boogaard, L., Gómez-López, J., et al. 2020, *ApJ*, 901, 79
- Astropy Collaboration, Price-Whelan, A. M., Lim, P. L., et al. 2022, *ApJ*, 935, 167
- Bacon, R., Brinchmann, J., Conseil, S., et al. 2023, *A&A*, 670, A4
- Barger, A. J., & Cowie, L. L. 2023, *ApJ*, 956, 95
- Barger, A. J., Cowie, L. L., Bauer, F. E., & González-López, J. 2019, *ApJ*, 887, 23
- Barger, A. J., Cowie, L. L., Blair, A. H., & Jones, L. H. 2022, *ApJ*, 934, 56
- Barger, A. J., Cowie, L. L., Sanders, D. B., et al. 1998, *Nature*, 394, 248
- Barger, A. J., Wang, W. H., Cowie, L. L., et al. 2012, *ApJ*, 761, 89
- Barger, A. J., Cowie, L. L., Chen, C. C., et al. 2014, *ApJ*, 784, 9
- Barrufet, L., Oesch, P. A., Weibel, A., et al. 2023, *MNRAS*, 522, 449
- Barrufet, L., Oesch, P. A., Marques-Chaves, R., et al. 2025, *MNRAS*
- Bell, E. F., Papovich, C., Wolf, C., et al. 2005, *ApJ*, 625, 23
- Bezanson, R., Labbe, I., Whitaker, K. E., et al. 2024, *ApJ*, 974, 92
- Boogaard, L. A., Gillman, S., Melinder, J., et al. 2024, *ApJ*, 969, 27
- Boquien, M., Burgarella, D., Roehlly, Y., et al. 2019, *A&A*, 622, A103
- Bouwens, R., González-López, J., Aravena, M., et al. 2020, *ApJ*, 902, 112
- Brammer, G. B., van Dokkum, P. G., & Coppi, P. 2008, *ApJ*, 686, 1503
- Bruzual, G., & Charlot, S. 2003, *MNRAS*, 344, 1000
- Bunker, A. J., Cameron, A. J., Curtis-Lake, E., et al. 2024, *A&A*, 690, A288
- Calzetti, D., Armus, L., Bohlin, R. C., et al. 2000, *ApJ*, 533, 682
- Caputi, K. I., Dunlop, J. S., McLure, R. J., et al. 2012, *ApJL*, 750, L20
- Carnall, A. C., McLure, R. J., Dunlop, J. S., & Davé, R. 2018, *MNRAS*, 480, 4379
- Chapman, S. C., Blain, A. W., Smail, I., & Ivison, R. J. 2005, *ApJ*, 622, 772
- Charlot, S., & Fall, S. M. 2000, *ApJ*, 539, 718
- Chen, C.-C., Cowie, L. L., Barger, A. J., et al. 2013, *ApJ*, 776, 131
- Chen, C.-C., Smail, I., Swinbank, A. M., et al. 2015, *ApJ*, 799, 194
- . 2016, *ApJ*, 831, 91
- Chen, C.-C., Gao, Z.-K., Hsu, Q.-N., et al. 2022, *ApJL*, 939, L7
- Cheng, C., Huang, J.-S., Smail, I., et al. 2023, *ApJL*, 942, L19
- Cowie, L. L., Barger, A. J., & Bauer, F. E. 2023, *ApJ*, 952, 28
- Cowie, L. L., Barger, A. J., Bauer, F. E., et al. 2022, *ApJ*, 939, 5
- Cowie, L. L., Barger, A. J., Hsu, L. Y., et al. 2017, *ApJ*, 837, 139
- Cowie, L. L., Barger, A. J., & Kneib, J. P. 2002, *AJ*, 123, 2197
- Cowie, L. L., González-López, J., Barger, A. J., et al. 2018, *ApJ*, 865, 106
- da Cunha, E., Charlot, S., & Elbaz, D. 2008, *MNRAS*, 388, 1595
- da Cunha, E., Walter, F., Smail, I. R., et al. 2015, *ApJ*, 806, 110
- Danielson, A. L. R., Swinbank, A. M., Smail, I., et al. 2017, *ApJ*, 840, 78
- D'Eugenio, F., Cameron, A. J., Scholtz, J., et al. 2024, arXiv e-prints, arXiv:2404.06531
- Draine, B. T., & Li, A. 2007, *ApJ*, 657, 810
- Dudzevičiūtė, U., Smail, I., Swinbank, A. M., et al. 2020, *MNRAS*, 494, 3828
- Dunlop, J. S., McLure, R. J., Biggs, A. D., et al. 2017, *MNRAS*, 466, 861
- Eales, S., Lilly, S., Gear, W., et al. 1999, *ApJ*, 515, 518
- Eisenstein, D. J., Willott, C., Alberts, S., et al. 2023a, arXiv e-prints, arXiv:2306.02465
- Eisenstein, D. J., Johnson, B. D., Robertson, B., et al. 2023b, arXiv e-prints, arXiv:2310.12340
- Elbaz, D., Dickinson, M., Hwang, H. S., et al. 2011, *A&A*, 533, A119
- Ferland, G. J., Chatzikos, M., Guzmán, F., et al. 2017, *RMxAA*, 53, 385
- Franco, M., Elbaz, D., Béthermin, M., et al. 2018, *A&A*, 620, A152
- Fujimoto, S., Bezanson, R., Labbe, I., et al. 2023, arXiv e-prints, arXiv:2309.07834

- Fujimoto, S., Kohno, K., Ouchi, M., et al. 2024, ApJS, 275, 36
- Furtak, L. J., Zitrin, A., Weaver, J. R., et al. 2023a, MNRAS, 523, 4568
- Furtak, L. J., Zitrin, A., Plat, A., et al. 2023b, ApJ, 952, 142
- Garilli, B., McLure, R., Pentericci, L., et al. 2021, A&A, 647, A150
- Gillman, S., Gullberg, B., Brammer, G., et al. 2023, A&A, 676, A26
- Gillman, S., Smail, I., Gullberg, B., et al. 2024, A&A, 691, A299
- Gómez-Guijarro, C., Elbaz, D., Xiao, M., et al. 2022, A&A, 658, A43
- González-López, J., Bauer, F. E., Romero-Cañizales, C., et al. 2017, A&A, 597, A41
- González-López, J., Decarli, R., Pavesi, R., et al. 2019, ApJ, 882, 139
- Gottumukkala, R., Barrufet, L., Oesch, P. A., et al. 2024, MNRAS, 530, 966
- Greene, J. E., Labbe, I., Goulding, A. D., et al. 2024, ApJ, 964, 39
- Hatsukade, B., Kohno, K., Yamaguchi, Y., et al. 2018, PASJ, 70, 105
- Hodge, J. A., Cunha, E. d., Kendrew, S., et al. 2025, ApJ, 978, 165
- Hopkins, P. F., Hernquist, L., Cox, T. J., & Kereš, D. 2008, ApJS, 175, 356
- Hsu, L.-Y., Cowie, L. L., Chen, C.-C., Barger, A. J., & Wang, W.-H. 2016, ApJ, 829, 25
- Hughes, D. H., Serjeant, S., Dunlop, J., et al. 1998, Nature, 394, 241
- Illingworth, G., Magee, D., Bouwens, R., et al. 2016, arXiv e-prints, arXiv:1606.00841
- Inami, H., Bacon, R., Brinchmann, J., et al. 2017, A&A, 608, A2
- Jain, R., & Wadadekar, Y. 2024, arXiv e-prints, arXiv:2412.04834
- Kamieneski, P. S., Frye, B. L., Pascale, M., et al. 2023, ApJ, 955, 91
- Kartaltepe, J. S., Rose, C., Vanderhoof, B. N., et al. 2023, ApJL, 946, L15
- Kennicutt, Robert C., J. 1998, ARA&A, 36, 189
- Knudsen, K. K., van der Werf, P. P., & Kneib, J. P. 2008, MNRAS, 384, 1611
- Kocevski, D. D., Finkelstein, S. L., Barro, G., et al. 2024, arXiv e-prints, arXiv:2404.03576
- Kokorev, V., Fujimoto, S., Labbe, I., et al. 2023, ApJL, 957, L7
- Kriek, M., Shapley, A. E., Reddy, N. A., et al. 2015, ApJS, 218, 15
- Kroupa, P. 2001, MNRAS, 322, 231
- Kurk, J., Cimatti, A., Daddi, E., et al. 2013, A&A, 549, A63
- Labbe, I., Greene, J. E., Bezanson, R., et al. 2025, ApJ, 978, 92
- Le Bail, A., Daddi, E., Elbaz, D., et al. 2024, A&A, 688, A53
- Le Fèvre, O., Tasca, L. A. M., Cassata, P., et al. 2015, A&A, 576, A79
- Lim, C.-F., Wang, W.-H., Smail, I., et al. 2020, ApJ, 889, 80
- Lo Faro, B., Buat, V., Roehlly, Y., et al. 2017, MNRAS, 472, 1372
- Manning, S. M., Casey, C. M., Zavala, J. A., et al. 2022, ApJ, 925, 23
- Matthee, J., Naidu, R. P., Brammer, G., et al. 2024, ApJ, 963, 129
- McKay, S. J., Barger, A. J., & Cowie, L. L. 2024, ApJ, 962, 128
- McKay, S. J., Barger, A. J., Cowie, L. L., Bauer, F. E., & Rosenthal, M. J. N. 2023, ApJ, 951, 48
- McKinney, J., Casey, C. M., Long, A. S., et al. 2025, ApJ, 979, 229
- McLure, R. J., Pentericci, L., Cimatti, A., et al. 2018, MNRAS, 479, 25
- Meyer, R. A., Barrufet, L., Boogaard, L. A., et al. 2024, A&A, 681, L3
- Michałowski, M. J., Hayward, C. C., Dunlop, J. S., et al. 2014, A&A, 571, A75
- Mignoli, M., Cimatti, A., Zamorani, G., et al. 2005, A&A, 437, 883
- Mihos, J. C., & Hernquist, L. 1996, ApJ, 464, 641
- Momcheva, I. G., Brammer, G. B., van Dokkum, P. G., et al. 2016, ApJS, 225, 27
- Muñoz Arancibia, A. M., González-López, J., Ibar, E., et al. 2023, A&A, 675, A85
- Naidu, R. P., Oesch, P. A., Setton, D. J., et al. 2022, arXiv e-prints, arXiv:2208.02794
- Naidu, R. P., Matthee, J., Kramarenko, I., et al. 2024, arXiv e-prints, arXiv:2410.01874
- Nardiello, D., Bedin, L. R., Burgasser, A., et al. 2022, MNRAS, 517, 484
- Nedkova, K. V., Rafelski, M., Teplitz, H. I., et al. 2024, ApJ, 970, 188
- Nelson, E. J., Suess, K. A., Bezanson, R., et al. 2023, ApJL, 948, L18
- Oesch, P. A., Brammer, G., Naidu, R. P., et al. 2023, MNRAS, 525, 2864
- Oke, J. B., & Gunn, J. E. 1983, ApJ, 266, 713

- Oliver, S. J., Bock, J., Altieri, B., et al. 2012, MNRAS, 424, 1614
- Pacifci, C., Iyer, K. G., Mobasher, B., et al. 2023, ApJ, 944, 141
- Padilla, N. D., & Strauss, M. A. 2008, MNRAS, 388, 1321
- Paris, D., Merlin, E., Fontana, A., et al. 2023, ApJ, 952, 20
- Peng, C. Y., Ho, L. C., Impey, C. D., & Rix, H.-W. 2002, AJ, 124, 266
- . 2010, AJ, 139, 2097
- Pentericci, L., McLure, R. J., Garilli, B., et al. 2018, A&A, 616, A174
- Pérez-González, P. G., Barro, G., Annunziatella, M., et al. 2023, ApJL, 946, L16
- Pérez-González, P. G., Rinaldi, P., Caputi, K. I., et al. 2024, ApJL, 969, L10
- Polletta, M., Frye, B. L., Garuda, N., et al. 2024, A&A, 690, A285
- Price, S. H., Bezanson, R., Labbe, I., et al. 2024, arXiv e-prints, arXiv:2408.03920
- Price, S. H., Suess, K. A., Williams, C. C., et al. 2025, ApJ, 980, 11
- Roper, W. J., Lovell, C. C., Vijayan, A. P., et al. 2022, MNRAS, 514, 1921
- Sanders, D. B., & Mirabel, I. F. 1996, ARA&A, 34, 749
- Smail, I., Ivison, R. J., & Blain, A. W. 1997, ApJL, 490, L5
- Stach, S. M., Dudzevičiūtė, U., Smail, I., et al. 2019, MNRAS, 487, 4648
- Sun, F., Egami, E., Fujimoto, S., et al. 2022, ApJ, 932, 77
- Sun, F., Helton, J. M., Egami, E., et al. 2024a, ApJ, 961, 69
- Sun, F., Wang, F., Yang, J., et al. 2025, ApJ, 980, 12
- Sun, W., Ho, L. C., Zhuang, M.-Y., et al. 2024b, ApJ, 960, 104
- Suzuki, T. L., van Mierlo, S. E., & Caputi, K. I. 2023, ApJ, 959, 82
- Swinbank, A. M., Smail, I., Chapman, S. C., et al. 2010, MNRAS, 405, 234
- Tan, Q.-H., Daddi, E., Magnelli, B., et al. 2024, Nature, 636, 69
- Targett, T. A., Dunlop, J. S., Cirasuolo, M., et al. 2013, MNRAS, 432, 2012
- Taylor, A. J., Finkelstein, S. L., Kocevski, D. D., et al. 2024, arXiv e-prints, arXiv:2409.06772
- Treu, T., Roberts-Borsani, G., Bradac, M., et al. 2022, ApJ, 935, 110
- Uematsu, R., Ueda, Y., Kohno, K., et al. 2024, ApJ, 965, 108
- van der Wel, A., Bell, E. F., Häussler, B., et al. 2012, ApJS, 203, 24
- van der Wel, A., Chang, Y.-Y., Bell, E. F., et al. 2014, ApJL, 792, L6
- Vanzella, E., Cristiani, S., Dickinson, M., et al. 2008, A&A, 478, 83
- Virtanen, P., Gommers, R., Oliphant, T. E., et al. 2020, Nature Methods, 17, 261
- Walter, F., Decarli, R., Aravena, M., et al. 2016, ApJ, 833, 67
- Wang, T., Elbaz, D., Schreiber, C., et al. 2016, ApJ, 816, 84
- Wang, T., Schreiber, C., Elbaz, D., et al. 2019, Nature, 572, 211
- Wang, W.-H., Barger, A. J., & Cowie, L. L. 2012, ApJ, 744, 155
- Weaver, J. R., Cutler, S. E., Pan, R., et al. 2024, ApJS, 270, 7
- Whitaker, K. E., Ashas, M., Illingworth, G., et al. 2019, ApJS, 244, 16
- Williams, C. C., Alberts, S., Ji, Z., et al. 2024, ApJ, 968, 34
- Wuyts, S., Förster Schreiber, N. M., van der Wel, A., et al. 2011, ApJ, 742, 96
- Xiao, M., Oesch, P. A., Elbaz, D., et al. 2024, Nature, 635, 311
- Xiao, M. Y., Elbaz, D., Gómez-Guijarro, C., et al. 2023, A&A, 672, A18
- Yamaguchi, Y., Kohno, K., Hatsukade, B., et al. 2019, ApJ, 878, 73
- Yan, H., Sun, B., & Ling, C. 2024, ApJ, 975, 44
- Zavala, J. A., Casey, C. M., Manning, S. M., et al. 2021, ApJ, 909, 165
- Zavala, J. A., Buat, V., Casey, C. M., et al. 2023, ApJL, 943, L9
- Zhuang, M.-Y., & Shen, Y. 2024, ApJ, 962, 139